

Copyright  
by  
Emek Yesilada  
2004

The Dissertation Committee for Emek Yesilada  
certifies that this is the approved version of the following dissertation:

## Excitations of Quantum Gases in Optical Lattices

Committee:

---

Daniel J. Heinzen, Supervisor

---

Manfred Fink

---

Greg O. Sitz

---

Denis A. Kohl

---

James L. Erskine

# Excitations of Quantum Gases in Optical Lattices

by

Emek Yesilada, B.S.

**DISSERTATION**

Presented to the Faculty of the Graduate School of  
The University of Texas at Austin  
in Partial Fulfillment  
of the Requirements  
for the Degree of

**DOCTOR OF PHILOSOPHY**

THE UNIVERSITY OF TEXAS AT AUSTIN

December 2004

To my wife Andrea,  
To my parents Ali Fevzi and Müzeyyen  
and my brothers Yasa and Can

## Acknowledgments

I would like to thank Dr. Daniel Heinzen for accepting me into his group from the first day of my graduate school. His vision of always pursuing the most challenging and interesting science helped me learn and explore the boundaries of physics. I have to say almost all of what I know about physics I learned in Dr. Heinzen's group.

During my first three years in graduate school I worked together with Dr. Gang Xu who is a true scientist. He never failed to answer my long list of questions and taught me all the basics I needed to become an experimental physicist. His role was really crucial in my training and I have to give him special thanks for that. Other senior students in the laboratory Dr. Roahn Wynar and Dr. Riley Freeland were always willing to help. Todd Goyen an undergraduate student when I first joined the group had great experimental skills and helped me with a lot of the early projects. Nathan Harrison made the daily life in the laboratory enjoyable from the treats he had on his desk to the music he played. He was also very good in tackling projects necessary to get the experiment going. I also want to thank Melanie Kittle for getting all the orders in quickly and Laura Feeney who are valuable members of the group.

During my last year I worked together with Dr. Changyun Ryu and

post-doc Dr. Xu Du. Chang had great intuition and taught me all the details of the new apparatus that helped me finish my project. Without Du's participation the experiment would be impossible to run. His hard work and patience helped reach the finish line. Shoupu Wan is the heir of the big experiment. His intelligence and computer skills were really handy in analyzing our data. I am sure he will lead many successful experiments during my absence.

Jack Clifford made the machine shop experience both instructive and fun. The staff on the fifth floor always had a solution to my needs.

Austin experience was much more than I thought thanks to many friends.

My parents support was really crucial to get me going through the harder days of my graduate school. Their hard work and dedication to their children cannot be put in words. Also my brother Yasa never spared any sacrifice to make sure I was not in need of anything. My younger brother Can visited me for a whole summer that allowed me to stay connected with the family.

Lastly, but most I want to thank my wife Andrea. She is the most incredible person I have met. Her understanding, patience and loving kept me going when life seemed difficult. I aspire to improve myself everyday to be worthy of her love. Thank you for everything. I also want to thank my mother in law Patricia for giving me her support and daughter.

**Emek Yesilada**

# Excitations of Quantum Gases in Optical Lattices

Publication No. \_\_\_\_\_

Emek Yesilada, Ph.D.

The University of Texas at Austin, 2004

Supervisor: Daniel J. Heinzen

This thesis describes experiments that studied the excitations of an ultra-cold atomic Rb gas in an optical lattice using Bragg spectroscopy. A Bose-Einstein condensate (BEC) of  $^{87}\text{Rb}$  was formed in a cloverleaf trap. An optical lattice of cubic symmetry, formed by the interference of six laser beams, was superimposed on the Rb BEC and turned on adiabatically. Such a system is well described by the Bose-Hubbard model, which predicts a quantum phase transition from a superfluid to a Mott insulator state at a critical lattice depth.

In the first experiment, we studied the superfluid regime. The superfluid admits sound waves as phonon excitations. In two photon Bragg spectroscopy two laser beams intersecting at angle on the condensate create such excitations. The excitation spectrum of BEC was measured in a three dimensional optical lattice as a function of lattice strength.

In the second experiment we studied the excitation spectrum of the Mott insulator. The lowest energy excitations in such a system are particle-hole excitations. These correspond to the hopping of atoms from one lattice site to another. The insulating phase is characterized by a gap in the excitation spectrum and we measured this particle-hole gap by Bragg spectroscopy. The precise nature of our measurement allowed us to study the opening of the excitation gap that has previously eluded experimental verification.



# Table of Contents

<b>Acknowledgments</b>	<b>v</b>
<b>Abstract</b>	<b>vii</b>
<b>List of Tables</b>	<b>xi</b>
<b>List of Figures</b>	<b>xii</b>
<b>Chapter 1. Introduction</b>	<b>1</b>
1.1 Weakly Interacting Regime . . . . .	2
1.2 Strongly Interacting Regime . . . . .	3
1.3 Probing quantum phase transitions . . . . .	5
1.4 Main results of this work . . . . .	6
<b>Chapter 2. Superfluid in optical lattices</b>	<b>7</b>
2.1 Excitations of Superfluid . . . . .	7
2.2 Bragg Spectroscopy . . . . .	8
2.2.1 Structure Factor and the Bogoliubov Theory . . . . .	11
2.2.2 Speed of Sound . . . . .	14
2.3 Excitations of the Superfluid in Optical Lattices . . . . .	15
2.3.1 Ultracold atoms in Optical Lattices . . . . .	15
2.3.2 Bloch Bands . . . . .	17
2.3.3 Structure Factor and Bogoliubov Theory in Optical Lattices	18
2.4 Experiment Setup . . . . .	20
2.4.1 Experimental Procedure . . . . .	20
2.4.2 Imaging System . . . . .	24
2.4.3 Atomic Source . . . . .	27
2.4.4 Laser Set Up . . . . .	29
2.4.5 Cooling Water . . . . .	32
2.5 Measurement of the Excitation Spectrum in Optical Lattices .	34

<b>Chapter 3. Mott Insulator</b>	<b>43</b>
3.1 Quantum phase transition from a Bose-Hubbard model . . . . .	44
3.1.1 Probing Phase Transition with Momentum Distribution . . . . .	49
3.2 Excitations in the Mott Insulator . . . . .	52
3.3 Preparing the Mott Insulator . . . . .	61
3.3.1 Loading Atoms into the Optical Lattice . . . . .	61
3.3.2 Calibration of the Optical Lattice . . . . .	64
3.4 Probing the Phase Transition with Bragg Spectroscopy . . . . .	65
3.4.1 Bragg Spectroscopy of the Mott Insulator . . . . .	66
3.5 Photoassociation Experiments in the Mott Insulator . . . . .	77
3.5.1 Single Photon Photoassociation of Mott Insulator . . . . .	77
3.5.2 Raman Photoassociation of a Mott Insulator . . . . .	78
 <b>Chapter 4. Conclusion</b>	 <b>86</b>
 <b>Appendix</b>	 <b>88</b>
 <b>Appendix 1. Lithium Setup</b>	 <b>89</b>
1.1 Two Species . . . . .	89
1.2 Lithium Laser System . . . . .	90
1.3 Two Species Zeeman Slower . . . . .	93
1.4 Loading the Two-Species Source into the Chamber . . . . .	95
 <b>Bibliography</b>	 <b>98</b>
 <b>Vita</b>	 <b>107</b>

## List of Tables

3.1	The parameters for different lattice strength . . . . .	64
-----	---	----

## List of Figures

2.1	Two Photon Bragg Spectrescopy . . . . .	10
2.2	Experiment chamber schematic . . . . .	21
2.3	Imaging lens tube and re-entrant window . . . . .	28
2.4	Drawing of dual species atoms source . . . . .	30
2.5	Bragg Spectroscopy laser beams set up . . . . .	33
2.6	3-D optical lattice set up . . . . .	39
2.7	Out coupled atoms . . . . .	40
2.8	Resonant response of superfluid to Bragg pulses . . . . .	41
2.9	Dispersion relation and speed of sound in 3D Lattice . . . . .	42
3.1	Bose Hubbard Phase Diagram . . . . .	47
3.2	Interference peaks . . . . .	53
3.3	Width of interference peaks . . . . .	54
3.4	Central peak width . . . . .	55
3.5	On site interaction energy . . . . .	56
3.6	Bose Hubbard Phase Diagram illustrating inhomegeneous trap	60
3.7	Bragg Response around Superfluid-Mott Insulator Transition .	70
3.8	Bragg Response around Superfluid-Mott Insulator Transition .	71
3.9	Bragg Response in Mott Insulator . . . . .	72
3.10	Opening of the Mott Gap . . . . .	73
3.11	Bragg spectra before and after the transition . . . . .	74
3.12	Bragg schematic and the particle-hole gap fit . . . . .	75
3.13	Opening of the Mott Gap . . . . .	76
3.14	Single photon phtoassociation . . . . .	78
3.15	Two color Raman photoassociation schematic . . . . .	81
3.16	Raman Scan of Mott Insulator . . . . .	84
3.17	Rabi oscillations between atoms and molecules . . . . .	85

1.1	Lithium laser setup . . . . .	92
1.2	Zeeman slower field profile for lithium . . . . .	96

# Chapter 1

## Introduction

Experiments done with liquid  $^4\text{He}$  [1, 2] exhibited an anomalous behavior which became known as superfluidity. Two groups independently measured the resistance to the flow of liquid  $^4\text{He}$  in narrow channels. They have observed that, below a certain temperature the liquid flowed without resistance. This zero viscosity behavior gave superfluidity its name. Superfluids also exhibit other interesting phenomena such as, reduction of moment of inertia, persistent currents, collective modes and quantized vortices. Superfluidity was first attributed to Bose-Einstein Condensation (BEC) by London [3]. BEC was predicted by Albert Einstein [4], who developed the work of Bose on quantum statistics of photons [5]. Einstein studied the behavior of noninteracting bosonic atoms, and showed that below a critical temperature  $T_c$  a macroscopic fraction of the atoms should condense into the lowest energy state. London's idea that superfluidity is due to BEC was not universally accepted as it was believed that BEC would not be possible when inter-atomic interactions are present as is the case for liquid  $^4\text{He}$ . N.N. Bogoliubov studied a dilute gas of atoms with weak repulsive interactions obeying Bose statistics and showed that such a system can Bose condense and exhibit superfluidity [6]. However, liquid helium is a strongly interacting system limiting the number of atoms

in the lowest energy (zero-momentum) state. Neutron scattering experiments showed the presence of a condensation of about  $\approx 10\%$  of atoms in liquid helium [7]. This led to the search for weakly interacting Bose gases with higher BEC fractions. The experimental realization of dilute alkali gas BEC's [8, 9] finally provided the textbook example of a weakly interacting system. One question was whether the phenomena observed for liquid helium could also be observed in trapped gases. A series of experiments has shown that indeed trapped alkali gas BEC's [10–15] do exhibit superfluidity and are ideal systems to test superfluidity theories.

## 1.1 Weakly Interacting Regime

The dilute alkali gas BEC's are dilute in the sense that the average particle spacing is large compared to the characteristic interaction length. Gross-Pitaevskii equation (GPE) describes such a dilute system at zero temperature [16]. The GPE assumes all the atoms are in the ground state (100% condensate fraction) and neglects interaction induced correlations. In the Bogoliubov theory the interactions between the particles cause a small fraction of atoms to populate excited states, the population of which constitutes the depletion of the condensate. The GPE and Bogoliubov theory are adequate to explain the results of many experiments such as speed of sound in BEC [12], collective oscillations [10, 11] and quantized vortices [13, 14]. In fact, Gross Pitaevski theory was first developed to study vortex states in weakly interacting bosons. These experiments showed that BEC of alkali atoms were ideal to study the

properties of superfluid as they can be described well with the theory. In a dilute gas BEC the s-wave scattering length  $a_s$  determines the interactions between the atoms. The strength of interactions can be characterized by the ratio of the interaction energy to the kinetic energy needed to correlate atoms by bringing them within a distance of average particle spacing,  $\gamma = E_{int}/E_{KE}$  which for a given density  $n$  is

$$\gamma = \frac{gn}{\hbar^2 n^{2/3}/m} \approx a_s n^{1/3} \quad (1.1)$$

where  $g = 4\pi\hbar^2 a_s/m$  is the interaction strength in the mean field approach. For a dilute gas BEC the inter particle spacing  $n^{-1/3}$  is much larger than the scattering length  $a_s$ . Thus the ratio  $\gamma$  is very small corresponding to a weakly interacting system. After excellent agreement between the experiments and theory researchers wanted to push into the strongly interacting regime to understand superfluidity in more complex systems.

## 1.2 Strongly Interacting Regime

The strongly interacting regime in the context of BEC means that the interaction induced correlations play an important role in determining the properties of the system and it can no longer be explained by the simple mean field approach of GPE. The scattering length  $a_s$  in BEC can be increased by Feshbach resonance [17] which provides an obvious way to reach strong coupling regime [18, 19]. The problem with this method is the shortening of the BEC lifetime due to three body losses. Another method is to erect an opti-



cal lattice onto a BEC. An optical lattice, [20–22] produced by the standing waves of an off resonant laser, confines atoms at the nodes (or antinodes) due to the dipole force on the atoms [23]. The localization of the atoms increases the interactions between them at the same time reducing their kinetic energy. The atoms can move from one lattice site to the next by tunnelling which plays the role of the kinetic energy. Tunnelling and thus the kinetic energy is suppressed with increasing lattice strength. The strength of the lattice can be easily adjusted experimentally and allows us to study the system with increasing interactions. For such a system the ratio of  $E_{int}/E_{KE}$  is no longer given by eq. (1). As we will see in the following chapters a condensate in an optical lattice can easily reach the strong coupling regime even though  $a_s n^{1/3}$  is still much smaller than 1. Thus ultra-cold atoms loaded in optical lattices can be used to study many problems that have not been practical before. Examples include studying superfluidity in moderate to strongly interacting systems, quantum phase transitions and quantum computation. One of the biggest advantages of ultra-cold atoms in optical lattices is the ease with which the interactions between the atoms can be changed, making different regimes (weakly interacting to strongly interacting) easily accessible. The number of atoms in such a system along with their temperature can also be adjusted. Another advantage includes the defect and impurity-free nature of the lattice compared to solid-state and condensed-matter systems allowing precision measurements. For example Bloch oscillations were observed using Cs atoms loaded in an optical lattice [24] that could not be observed in solid crystals

before. Josephson oscillations were realized with a BEC in a one dimensional optical lattice [15]. Precision measurements such as Bragg spectroscopy done on BEC's [25] to measure the Bogoliubov excitation spectrum can be implemented with BEC's in optical lattices to measure the excitation spectrum of the BEC in the lattice. Last but not the least a quantum phase transition from a superfluid to a Mott-insulator was observed [28] in a remarkable experiment that triggered a surge of research both experimentally and theoretically to understand properties of condensates in optical lattices.

### **1.3 Probing quantum phase transitions**

Ultra-cold atoms in an optical lattice can be described with the Bose-Hubbard model [26]. This model described bosons in a lattice and was used to study liquid helium in porous media. Jaksch showed that ultra-cold atoms in optical lattices is a simple realization of the Bose-Hubbard model [27]. One of the peculiarities of this model is the prediction of a quantum phase transition from a superfluid to an insulating phase. Recently, an experiment realized such a quantum phase transition [28]. The onset of insulating phase is accompanied by a loss of coherence of the wave function of the superfluid. The loss of coherence can be probed with interference experiments and was realized in the original experiment by Greiner et al. [28] and also reproduced in our group. However, several processes can lead to a loss of coherence such as heating and depletion of the condensate, so loss of coherence alone is not proof of Mott insulating state. The other important feature of the Mott insulator state is

a gap in the excitation spectrum. Two different experiments were done to detect this gap in the excitation spectrum, by applying a potential gradient to the lattice [28], and shaking the lattice in one direction [29]. Although their spectra shows a gap, the nature of the opening of the gap close to the transition could not be probed. We use Bragg spectroscopy proposed by Oosten *et al.* [30] to measure the particle-hole gap associated with the Mott insulator phase and analyze the opening of the gap close to the transition.

## 1.4 Main results of this work

This thesis consists of two experiments. The first experiment consists of measuring the excitation spectrum of  $^{87}\text{Rb}$  condensate loaded in an optical lattice. We use Bragg spectroscopy to study the response of the system at varying lattice heights. Up to a certain lattice height the system is a superfluid and admits sound waves. We use Bragg spectroscopy similar to experiments done by D.M. Stamper *et al.* [25] on condensates to study excitations of superfluid in the lattice. We plot the excitation energy of the condensate as a function of lattice height. In the second experiment we perform Bragg spectroscopy in the Mott insulator phase. We measure the particle-hole gap in the excitation spectrum. We show that the particle-hole gap tends to the on-site interaction energy deep in the Mott insulator phase and decreases more rapidly as we approach the superfluid region as predicted by Oosten *et al.* [30].

## Chapter 2

### Superfluid in optical lattices

Much work has been done to understand the properties of a weakly interacting superfluids since the experimental realization of the dilute gas BEC. Quasi-particles, collective excitations, and speed of sound concepts were developed to try to describe the superfluidity since experiments on liquid Helium. The problem with liquid Helium is that it is strongly interacting and these interactions cannot be treated by simple mean-field approach as in the dilute BEC case. The weak interactions in the BEC allowed researchers to verify experimental results by theory and vice versa. The next question is to try to understand the behavior of superfluid with stronger interactions. Ultra-cold atoms loaded in optical lattices provide a unique way to study the behavior of the superfluid as a function of interaction strength between the atoms since we can change the interaction strength by changing the lattice strength.

#### 2.1 Excitations of Superfluid

As mentioned earlier, N. Bogoliubov gave the first macroscopic derivation of the elementary excitation spectrum of a weakly interacting Bose gas [6]. The excitation spectrum gives the energy  $\hbar\omega(q)$  as a function of its momentum

wave vector  $q$ . The elementary excitation spectrum has been measured in He II by neutron scattering [31]. The low momentum excitations are phonons corresponding to collective excitations of the system. The theory for interacting bosons can reliably only describe the case of dilute gases where the interactions are weak, as opposed to liquid He. The realization of dilute alkali gas BEC's [32, 33] allowed this theory to be tested experimentally for the first time. In the first experiments shape oscillations of BEC's that are analogous to phonons in homogeneous systems were studied [10, 11]. Speed of sound in BEC was first measured by exciting density perturbations and observing the propagation of sound waves by Ketterle's group [12]. The same group also used Bragg spectroscopy to study phonon modes of the BEC both in the interacting and free particle regime. Another experiment also utilized Bragg spectroscopy to map out the excitation spectrum of the BEC [35]. Thus, Bragg spectroscopy was proved to be a powerful tool to do precise measurement of excitations in the BEC. We use Bragg spectroscopy to study excitations of the BEC in the optical lattice.

## 2.2 Bragg Spectroscopy

Bragg scattering was first demonstrated by W. H. Bragg and W. L. Bragg in 1912 by scattering X-rays from crystal planes. Neutron and light scattering has been used in the past to study the excitations of liquid helium [31]. This provided a lot of insight into the properties of superfluid Helium such as the type of excitations in the system, an upper bound for the superfluid

critical velocity, and the structure factor (sec.2.2.1) of the superfluid. Thus, Bragg spectroscopy of dilute gas BEC is an appealing method to understand its properties. Bragg scattering of atoms from a standing light wave was first observed by Martin *et al.* [34]. Several experiments were done to study the properties of BEC using two-photon Bragg scattering [25, 35].

Bragg scattering of atoms involves coupling of the two momentum states of an atom via a stimulated two photon process. It can be thought of as a Raman process where two momentum states are coupled as opposed to the internal states of the atoms. Thus this stimulated two photon process is referred to as Bragg spectroscopy in analogy to Raman spectroscopy.

To perform Bragg spectroscopy the sample of interest is illuminated by two laser beams intersecting at an angle  $\theta$  as shown in Fig. 2.1. We require that the lasers are both far detuned from any optical transitions so that spontaneous scattering is suppressed. The relative detuning between the two lasers  $\omega = \omega_2 - \omega_1$  is adjustable and can be very small. When an atom absorbs a photon from one beam and is stimulated to emit another photon into the second beam, it acquires a momentum of  $\hbar\mathbf{q}$  and energy of  $\hbar\omega$  given by equations:

$$\hbar\mathbf{q} = \hbar\mathbf{k}_2 - \hbar\mathbf{k}_1 = 2\hbar\mathbf{k} \sin\left(\frac{\theta}{2}\right) \quad (2.1)$$

$$\hbar\omega = \hbar\omega_2 - \hbar\omega_1. \quad (2.2)$$

It was shown [25] that the two photon excitation rate  $R_{2p}$  per atom is given by

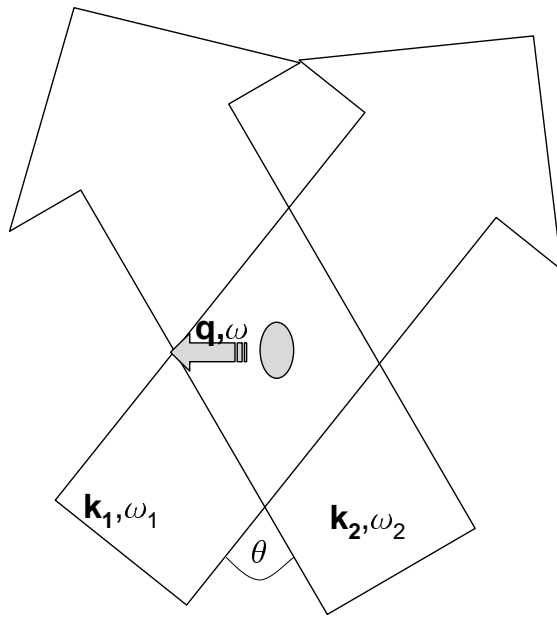


Figure 2.1: Bragg spectroscopy set-up. The momentum transfer is determined by the angle between the Bragg beams. The momentum transfer is determined by the angle  $\theta$  while the frequency difference  $\omega = \omega_2 - \omega_1$  determines the energy transfer.

$$R_{2p} = 2\pi\Omega_{2p}^2(S(\mathbf{q}, \omega) - S(-\mathbf{q}, -\omega)) \quad (2.3)$$

where  $\Omega_{2p}$  is the two photon Rabi frequency given by

$$\Omega_{2p} = \frac{\Gamma^2}{4\Delta} \frac{\sqrt{I_1 I_2}}{I_{sat}}. \quad (2.4)$$

$\Gamma$  is the line width of the relevant optical transition,  $\Delta$  is the detuning of the laser beams from this transition,  $I_1$ ,  $I_2$ , are the intensities of beams 1 and 2, and  $I_{sat}$  is the saturation intensity.

The dynamic structure factor  $S(\mathbf{q}, \omega)$  is a measure of the excitation of the density fluctuations and deserves detailed explanation.

### 2.2.1 Structure Factor and the Bogoliubov Theory

The dynamic structure factor characterizes the dynamic response of quantum many-body systems to a probe. It was first introduced to understand the measurement of the excitation spectrum of  ${}^4\text{He}$  [36]. For a many body system, the structure factor is defined as [31]

$$S(\mathbf{q}, \omega) = \frac{1}{Z} \sum_{mn} e^{-\beta E_m} |\langle m | \rho_{\mathbf{q}} | n \rangle|^2 \delta(E - E_m - E_n) \quad (2.5)$$

where  $\mathbf{q}$  is the wave vector of the momentum and  $E$  is the energy transferred to the system from the probe.  $E_n$  is the eigenvalue of the eigenstate  $|n\rangle$ ,  $\rho_{\mathbf{q}} = \sum_j e^{i\mathbf{q}\cdot\mathbf{r}_j/\hbar}$  is the Fourier transform of the single particle density operator, and  $Z$  is the canonical partition function. In two-photon Bragg spectroscopy the atoms can be scattered by absorbing a photon from either of the



laser beams. Therefore, what is measured in Bragg spectroscopy is actually  $(S(\mathbf{q}, \omega) - S(-\mathbf{q}, -\omega))$ . This is important because  $S(\mathbf{q}, \omega)$  has a temperature dependence that cancels out in the two photon case. Thus, one extracts the information of the zero temperature system even for finite temperatures in the BEC. This also means two photon Bragg spectroscopy is not a good tool to measure the temperature of a superfluid.

The energy of a free particle with momentum  $\hbar q$  is  $\hbar\omega_0 = \hbar^2 q^2 / 2m$ . If we perform Bragg spectroscopy on a sample of non-interacting free particles at rest, the particles will absorb photons and be stimulated to emit photons to the other beam at a frequency difference for which the momentum and energy is conserved, i.e the resonant frequency  $\omega$  will be  $\hbar q^2 / 2m$  corresponding to the recoil momentum. In the Bogoliubov approach the effect of repulsive interactions gives rise to an increase in the chemical potential  $\mu$ . Including the interactions between atoms the energy of the quasi-particle excitations becomes

$$\hbar\omega_B = \sqrt{\hbar\omega_0(\hbar\omega_0 + 2gn)} \quad (2.6)$$

where  $g = 4\pi\hbar^2 a_s / m$  with  $a_s$  the s wave scattering length. The product  $gn$  is usually denoted by  $U$ , the inverse compressibility, giving the strength of interactions between the atoms. For the high momentum case  $\hbar^2 q^2 / 2m \gg U$  the dispersion relation  $\hbar\omega_B = \hbar\omega_0 + U$  looks like that of free particles with the additional offset due the interactions. For low momentum,  $\hbar^2 q^2 / 2m \ll U$ , the dispersion relation becomes  $\hbar\omega_B = \hbar q \sqrt{U/m}$ . Note that for the low

momentum case the resonant excitations are linear in  $q$ , while in the high momentum case it is quadratic. The crossover from collective transitions to free particle like excitations occurs at momenta on the order of  $\hbar/\zeta$  where  $\zeta$  is a characteristic length called the healing length given by

$$\zeta = \frac{1}{8\pi n a_s} \quad (2.7)$$

Thus the nature of the excitations in the superfluid is strongly dependent on the wave vector  $q$  of the excitations. If we perform Bragg spectroscopy we should expect the resonance condition to change depending on the interactions in the system as given by the Bogoliubov dispersion relation. Stamper Kurn *et al.* has done Bragg spectroscopy with fixed  $q$  and demonstrated the shift in resonance frequency between a free particle-like and an interacting cloud [25]. Note also from eq. (2.1) that in Bragg spectroscopy  $q$  depends on the angle  $\theta$  between the two Bragg beams. Davidson *et al.* [35] has varied the angle  $\theta$  to change  $q$  and mapped out the excitation spectrum of the BEC from low  $q$  to high  $q$  where they were able to show the dispersion relation changing from linear to quadratic in  $q$ .

The integral of  $S(\mathbf{q}, \omega)$  over  $\omega$  gives the static structure factor  $S(\mathbf{q})$ , which is the Fourier transform of the density-density correlation function [31]. Thus  $S(\mathbf{q})$  measures the magnitude of the density fluctuations in the fluid. Stamper Kurn *et al.* [25] showed that using a Thomas Fermi density distribution for a BEC  $S(q) \rightarrow 15\pi/32(\hbar\omega_0/2\mu)^{1/2}$  for low  $q$  and  $S(q) \rightarrow 1 - 4\mu/7\hbar\omega_0$  for high  $q$ . This shows that the excitations are suppressed in the phonon

regime. This is attributed to the quantum depletion in the condensate [25].

The condensate can be described by the local density approximation as long as the Thomas Fermi radius in the  $\mathbf{q}$  direction is much bigger than the wavelength of the excitation [37]. Then the excitation spectrum is given by

$$\omega(q) = \sqrt{c_{LDA}(q)^2 q^2 + \left(\frac{\hbar q^2}{2m}\right)^2} \quad (2.8)$$

where  $c_{LDA}(q)$  is  $\frac{\hbar q}{2m} \sqrt{\frac{1}{S(q)^2} - 1}$  and the static structure factor  $S(q)$  is [25, 35, 37].

$$S(q) = \frac{15}{4} \left( \frac{3 + \alpha}{4\alpha^2} - \frac{3 + 2\alpha - 2\alpha^2}{16\alpha^{5/2}} \left( \pi + 2 \arctan\left(\frac{\alpha - 1}{2\sqrt{\alpha}}\right) \right) \right) \quad (2.9)$$

where  $\alpha = 2\mu/(\hbar^2 q^2/2m)$ . The value  $c_{LDA}(q)$  changes very slowly thus the excitation spectrum is well approximated by the Bogoliubov theory (eq. 2.6).

### 2.2.2 Speed of Sound

The speed of sound in the superfluid corresponds to the speed phonons (low  $q$  excitations) travel. This speed is equivalent to the slope of the excitation spectrum as a function of  $q$ . We have shown that for low  $q$  (dispersion relation linear in  $q$ ) this slope (the speed of sound) is given by

$$c = \sqrt{\frac{U}{m}} \quad (2.10)$$

The speed of sound is also known as the Bogoliubov sound in reference to his pioneering work that showed that phonons travel with speed  $c$  in weakly interacting bosons. This can be measured with low  $q$  excitations where the dispersion relation is linear in  $q$ . Steinheur *et al.* has measured the speed of sound with Bragg spectroscopy [35]. For low  $q$  the resonance frequency  $\omega(q)$  is given by the dispersion relation and one can readily obtain speed of sound from  $c = \omega(q)/q$ .

The question then arises as to the response of the superfluid to the excitations in the optical lattice. If the system is a superfluid it should admit sound waves. The observation of sound modes in a lattice that is not translationally invariant is due to the long range phase coherence of the superfluid. This means atoms move coherently through the lattice giving rise to dissipationless currents. The study of excitations in the optical lattice is the central theme of this thesis.

## 2.3 Excitations of the Superfluid in Optical Lattices

### 2.3.1 Ultracold atoms in Optical Lattices

Optical traps have been used to trap atoms for various experiments [38]. The simplest optical trap consists of a single Gaussian laser beam. A two-level atom with a separation of  $\hbar\omega_A$  between its levels, when exposed to such a beam experiences a force given by the potential [23, 39]

$$V = \frac{\hbar^2\Omega^2}{4\Delta} \tag{2.11}$$

where  $\Omega$  is the Rabi frequency, and  $\Delta = \omega_L - \omega_A$  is the detuning of the laser frequency  $\omega_L$  from the atomic resonance frequency  $\omega_A$ . The Rabi frequency  $\Omega$  is related to the intensity by  $\Omega^2 = \Gamma^2 I / 2I_s$ , where  $\Gamma$  is the decay rate of the excited level and  $I$  and  $I_s$  are the intensity of the laser beam and saturation intensity respectively. The atoms also spontaneously scatter photons from the laser beam at a rate

$$\gamma_s = \frac{\Gamma \Omega^2}{4\Delta^2}. \quad (2.12)$$

Spontaneous scattering causes heating of the atoms. For a multilevel atom all the relevant transitions need to be included for the calculation of the potential and the spontaneous scattering rate. Since  $\Omega^2$  is proportional to the laser intensity, we can increase the laser intensity as we increase  $\Delta$  to keep the same potential with a smaller  $\gamma_s$ .

A one dimensional (1D) optical lattice can be constructed by retro-reflecting a Gaussian laser beam. This will form a standing wave with periodic intensity modulations. The intensity of the standing wave is four times that of the incoming beam giving  $\Omega(x)^2 = 4\Omega^2 \sin^2(kx)$ . Thus, the potential for an atom in a 1D lattice is of the form

$$V_0(x) = 4V \sin^2(kx). \quad (2.13)$$

2D square lattices or 3D cubic lattices can be constructed by having 2 or 3 sets of orthogonal retro-reflecting beams. For a 3D lattice the potential at the trap center is of the form

$$V(x, y, z) = V_0[\sin^2(kx) + \sin^2(ky) + \sin^2(kz)]. \quad (2.14)$$

Note that these expressions are for a collimated beam. For Gaussian beams of waist  $\varpi$  the actual potential is of the form

$$V(x, y, z) = V_0[\sin^2(kx)e^{-2\frac{y^2+z^2}{\varpi_x^2}} + \sin^2(ky)e^{-2\frac{x^2+z^2}{\varpi_y^2}} + \sin^2(kz)e^{-2\frac{x^2+y^2}{\varpi_z^2}}]. \quad (2.15)$$

In experiments the waist of the gaussian beams are much bigger than the size of the sample, so for small distances around the trap center this potential can be approximated by

$$V(x, y, z) = V_0[\sin^2(kx) + \sin^2(ky) + \sin^2(kz)] + \frac{1}{2}m[\omega_{xL}^2x^2 + \omega_{yL}^2y^2 + \omega_{zL}^2z^2] \quad (2.16)$$

where  $\omega_{xL}, \omega_{yL}, \omega_{zL}$  are the quadratic trap frequency contributions of the laser beams given by

$$\omega_{iL} = \sqrt{\frac{4}{4}\left(\frac{V_j}{\varpi_y^2} + \frac{V_k}{\varpi_k^2}\right)}. \quad (2.17)$$

In our experiments  $V_x = V_y = V_z = V_0$  which is expressed in terms of the recoil energy  $E_r = \hbar^2k^2/2m$ . It should be also mentioned that if the beams in different axis have the same frequency there will be interference between them which will modify the potential. This problem can be avoided by using orthogonal polarizations and/or different frequencies for each axis.

### 2.3.2 Bloch Bands

The periodic potential of the lattice results in the appearance of a band structure as in solid state systems. The eigenstates of a Hamiltonian with a periodic potential are Bloch functions of the form

$$\Phi_{jq}(x) = e^{iqx} u_{jq}(x) \quad (2.18)$$

where  $u_{jq}(x)$  has the same periodicity as the potential. For an optical lattice constructed from a laser with wavelength  $\lambda$  the lattice constant is  $\lambda/2$  and we require  $u_{jq}(x) = u_q(x + \lambda/2)$ . For a 1D lattice this wave function can be inserted into the Schrödinger equation to get the band structure of an atom in a periodic lattice. We can express the strength of an optical lattice in terms of the recoil energy  $E_r = \hbar^2 k^2 / 2m$ . In a deep lattice where  $V_0 \gg E_r$  each lattice site can support many vibrational levels. We would like the atoms to stay in the lowest energy band. If the lattice is turned on too fast the atoms can populate higher energy bands. The time scale for adiabaticity (to stay in the first band) is roughly  $(E_n - E_0)/\hbar$ , where  $E_n$  is the  $n$ th band and  $E_0$  is the first band. This time scale is less than a millisecond and is satisfied easily. There is another condition for staying in the ground state of the system that is related to the tunnelling of the atoms which is harder to satisfy and will be discussed in section 3.3.2.

### 2.3.3 Structure Factor and Bogoliubov Theory in Optical Lattices

As stated in sect. 2.2.1 for a BEC the static structure factor  $S(\mathbf{q})$  is affected by the phonon correlations due to the interactions between the atoms. The static structure factor of the BEC in a 1D lattice was studied and it was shown that its behavior is dominated by the phonon correlations giving [41]

$$S(q) \rightarrow \frac{|\hbar q|}{2m^*c} (\text{for } q \rightarrow 0) \quad (2.19)$$

where  $m^*$  is the effective mass and  $c$  is the speed of sound in the lattice. The effective mass is defined as the curvature of the lowest Bloch band. An approximate expression for the case of high lattice heights ( $V_0 \gg E_r$ ) was given by Zwerger [40]

$$m^* \approx \frac{2\hbar^2}{\lambda^2 J} \quad (2.20)$$

where the bandwidth  $J$  is the gain in kinetic energy due to tunnelling. Using the 1-D Mathieu equation an expression for  $J$  in the  $V \gg E_r$  limit can be obtained [40]

$$J = E_r \frac{4}{\sqrt{\pi}} \left(\frac{V_0}{E_r}\right)^{3/4} e^{-2\sqrt{\frac{V_0}{E_r}}}. \quad (2.21)$$

We can also write an expression for the speed of sound  $c$  in the lattice as

$$c = \sqrt{\frac{1}{\kappa m^*}} \quad (2.22)$$

where the  $\kappa = (n\partial\mu/\partial n)^{-1}$  is the inverse compressibility. The inverse compressibility depends on the chemical potential  $\mu$  determined by the interactions between the atoms and reduces to  $1/gn$  for no lattice. While the interaction between the atoms is increasing,  $m^*$  is increasing exponentially and the competition between the two processes determines the Bogoliubov sound in the lattice for low  $q$ . We note that for zero lattice height  $m^* = m$  and we recover the speed of sound without the lattice. While it is easy to obtain analytic expressions for the effective mass and inverse compressibility in the case of strong lattice (tight binding regime) these quantities need to be computed for smaller lattice strengths. There have been some calculations showing a



decreasing speed of sound as the lattice is raised in one-dimensional lattices [41]. Another paper by de Boer argues that for low lattice heights even though the 1D case shows a monotonic decrease in the speed of sound, a 3D lattice exhibits an increase in  $c$  before starting to go down [42]. This is due to the fact that for low lattice heights, the interactions between the atoms is increasing faster than the effective mass.

We use Bragg spectroscopy to find the resonance for different lattice heights in the low  $q$  regime. This corresponds to mapping the Bogoliubov excitation spectrum for a fixed  $q$  as a function of lattice strength.

## 2.4 Experiment Setup

### 2.4.1 Experimental Procedure

The experimental apparatus is discussed in detail in [51] and here I give an overview of the apparatus and the changes we have made. This apparatus has the ability to produce a few million atom BEC's within hours of turning on the experiment. The ease of producing a BEC reliably allows us perform complicated experiments where BEC is the starting point. The experiment is carried out in an ultra-high vacuum chamber which is separated into the atom source side and the experiment chamber by a gate valve. A schematic of the experimental apparatus is shown in Fig. 2.2.

The production of the BEC starts from slowing an atomic beam of  $^{87}\text{Rb}$  using a Zeeman slower [43] and a slower laser beam detuned 1.492 GHz to the red of the  $5S_{1/2}(F = 2) \rightarrow 5P_{3/2}(F = 2)$  transition, counter prop-

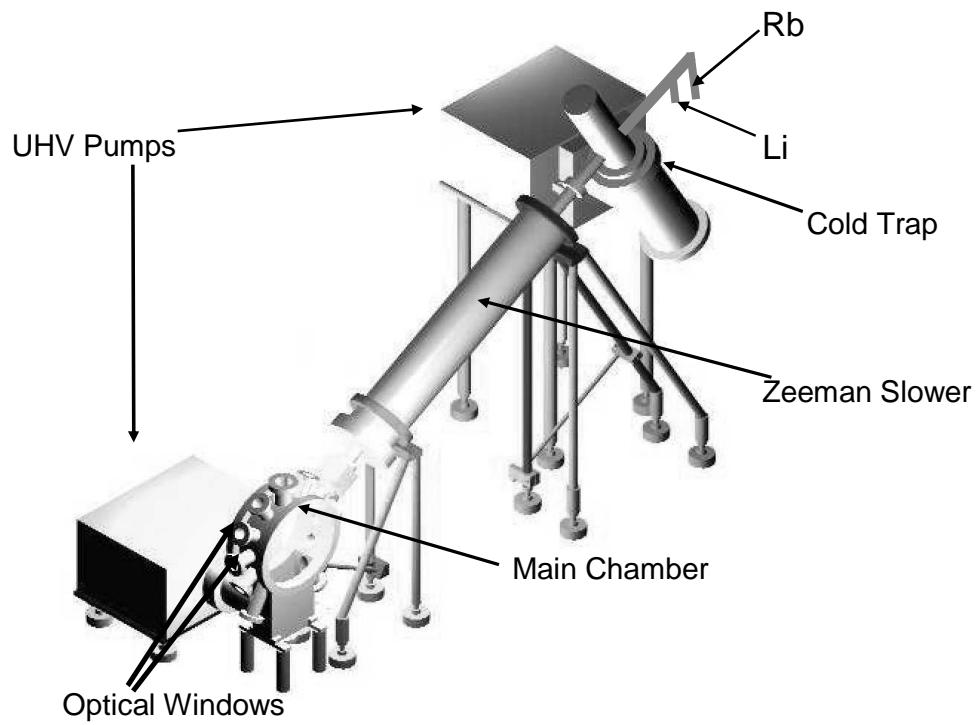


Figure 2.2: Schematic drawing of the experiment chamber showing dual species atom source, the zeeman slower, support structure, the ion pumps and the main chamber.

agating the atomic beam. The slowed atoms are loaded into a magneto-optical trap (MOT) employing a trapping laser locked to 15 MHz red of the  $5S_{1/2}(F = 2) \rightarrow 5P_{3/2}(F = 3)$  and a repumper laser locked to the  $5S_{1/2}(F = 1) \rightarrow 5P_{3/2}(F = 2)$  transition. After about 30 s of MOT loading we can get about  $5 \times 10^9$  atoms. The density of the atoms in the MOT is limited due to radiative repulsion [44]. This limitation is overcome by transferring atoms into a dark MOT [45] by putting a hole in the center of the repumper beam such that in the absence of repumper beam atoms do not absorb any photons. Densities of  $2 \times 10^{11} \text{ cm}^{-3}$  are achieved after 150ms in the dark MOT at which point the temperature of the atomic cloud is down to  $180 \mu\text{K}$ . To reduce the temperature of the cloud further a 5ms molasses is applied during which the MOT coils are turned off and only MOT trapping beams are on with a detuning of -35 MHz from the  $5S_{1/2}(F = 2) \rightarrow 5P_{3/2}(F = 3)$ . After molasses we end up with a cloud density of  $\approx 10 \times 10^{10} \text{ cm}^{-3}$  and a temperature of  $\approx 50 \mu\text{K}$  that is ready to be transferred into a magnetic trap. The magnetic trap is a Ioffe-Pritchard type trap [46, 47] that produces a harmonic confinement with a bias field in the center to avoid Majorana spin flips [48]. The atoms are optically pumped into the  $|F = 1, m_F = -1\rangle$  state and the magnetic trap is suddenly turned on yielding a trap frequency of 9Hz for this atomic state, in order to match the atomic cloud size to the trap geometry. The magnetic trap frequencies are then increased adiabatically to their maximum values of 11.6 Hz for the axial direction and 170.5 Hz for the radial direction in order to maximize the elastic scattering in evaporation. In order to reach the quantum

degenerate regime the atomic cloud is cooled further using forced evaporative cooling. This process involves radio-frequency (RF) induced transitions between Zeeman levels of energetic atoms and untrapped states. The RF field is generated by a rectangular RF coil inside the chamber. We start with a radio-frequency of 30 MHz to selectively transfer atoms with energy higher than average to untrappable states. The remaining atoms rethermalize at a lower temperature. This process is continued for 20s by decreasing the RF amplitude and frequency. At the end of the evaporation we can obtain pure condensates of up to  $2 \times 10^6$  Rb atoms in the  $|F = 1, m_F = -1 \rangle$ . The temperature of the atomic cloud can be inferred from its density profile that has a temperature dependence.

A thermal cloud (not a condensate) of  $N$  atoms at a temperature  $T$ , has a Gaussian density profile given by

$$n(r, z)_{th} = n_{th}^0 e^{(-\frac{r^2}{r_{th}^2} - \frac{z^2}{z_{th}^2})} \quad (2.23)$$

where

$$r_{th} = \sqrt{\frac{2k_B T}{m} \frac{1}{\omega_r^2}}, z_{th} = \sqrt{\frac{2k_B T}{m} \frac{1}{\omega_z^2}} \quad (2.24)$$

are the radial and axial cloud sizes, depending on the radial and axial trap frequencies  $\omega_r$  and  $\omega_z$ , respectively. The peak density in the trap center is  $n_{th}^0 = N\pi^{-3/2}/r_{th}^2 z_{th}$ . During evaporation, the atomic cloud goes through a phase transition into the BEC at a temperature

$$T_c = \frac{\hbar\omega}{k_B} \left(\frac{N}{1.202}\right)^{1/3} \quad (2.25)$$

where  $w = (\omega_r^2 \omega_z)^{1/3}$ . The Bose condensed cloud can be described by the Thomas-Fermi approximation [49] where the kinetic energy is ignored due to being negligible compared to the trap and self energy. In the Thomas Fermi limit the BEC density profile takes the shape of an inverted parabola

$$n_c(r, z) = n_c^0 \left( 1 - \frac{r^2}{r_{TF}^2} - \frac{z^2}{z_{TF}^2} \right) \quad (2.26)$$

where

$$n_c^0 = \frac{\mu}{g}. \quad (2.27)$$

The interaction strength  $g = 4\pi\hbar^2 a_s/m$  and the chemical potential  $\mu$  is given by

$$\mu = \frac{1}{2} m^{1/5} (15 N a_s \hbar^2 w^3)^{2/5}. \quad (2.28)$$

We can detect the density profile of the condensate by optical imaging that is covered in detail in next section.

### 2.4.2 Imaging System

Our main detection of the condensate is done by absorption imaging. If atoms are illuminated by a resonant or near resonant light beam, they absorb some of the light and cast a shadow. A probe light with intensity  $I_0(x, y)$  will be attenuated after passing through the cloud. The attenuation depends on the optical density  $D(x, y)$  of the cloud such that the intensity of the emerging probe light is

$$I(x, y) = I_0(x, y) e^{-D(x, y)}. \quad (2.29)$$

The optical density is the product of the column density  $\bar{n}(x, y)$  and the absorption cross section  $\sigma$ . The column density is the integral of the spatial density along the propagation axis of the probe beam

$$\bar{n}(x, y) = \sigma \int n(x, y, z) dz \quad (2.30)$$

and

$$\sigma = \sigma_0 \frac{1}{1 + \frac{4\Delta^2}{\Gamma^2} + \frac{I}{I_{SAT}}} \quad (2.31)$$

where  $\sigma_0 = 3\lambda^2/2\pi$  is the resonant cross section,  $\Delta$  is the detuning of the probe light,  $\Gamma$  is the natural line width of the transition and  $I_{SAT}$  is the saturation intensity.

We take an absorption image of the cloud after the trap is switched off and the cloud is allowed to expand called time of flight (TOF) image. The main reason for using this method is that the optical density  $D$  of the condensate is too high before expansion. To take a TOF image the trap needs to be switched off fast enough so that the system is not evolving during the switch off. The relevant time scale is the trapping frequency. For the magnetic trap the trapping frequencies are in the range of 10-200 Hz. The magnetic trap can be turned off in 1.5 ms limited by the Eddy currents which is fast enough. For atoms in the optical lattice the local trapping frequencies of individual sites are on the order of 10 kHz. However, the optical lattice field is switched off in less than a  $\mu s$  using an AOM allowing a snap-shot of the cloud. During the free expansion, a thermal cloud expands as

$$x_{th} = \frac{2k_B T}{m} \left( \frac{1}{\omega_x^2 + t^2} \right) \quad (2.32)$$

whereas a condensate expands as

$$x_c = \lambda_x(\tau) \sqrt{\frac{2\mu}{m\omega_x^2}} \quad (2.33)$$

where  $x$  is either  $r$  or  $z$ ,  $C$  is the expansion coefficient from conversion of self energy to kinetic energy, and  $\tau = t\omega_r$  is the time scaling factor. The coefficients are from Castin and Dum model of an expanding condensate [50], and are obtained by fitting the solutions of the following coupled differential equations

$$\frac{\partial^2 \lambda_r}{\partial \tau^2} = \frac{1}{\lambda_r^3 \lambda_z}, \quad (2.34)$$

$$\frac{\partial^2 \lambda_z}{\partial \tau^2} = \frac{\epsilon^2}{\lambda_r^2 \lambda_z^2}. \quad (2.35)$$

The two differential equations must satisfy the boundary conditions  $\lambda_x(0) = 1$  and  $\partial \lambda_x / \partial \tau|_{\tau=0} = 0$ . Using eq. 2.29 the images cloud can be expressed as the sum of a condensate and a thermal cloud

$$S = -\ln \frac{I}{I_0} = S_c(x, y) + S_{th}(x, y) \quad (2.36)$$

where

$$S_c(x, y) = \frac{4}{3} \frac{\sigma N_c r_c}{\lambda_r(t) \lambda_z(t)} \left( 1 - \frac{x^2}{\lambda_r^2(t) r_c^2} - \frac{y^2}{\lambda_z^2(t) z_c^2} \right)^{3/2} \quad (2.37)$$

and

$$S_{th}(x, y) = \frac{N_{th}}{\pi r_{th}(t) z_{th}(t)} \exp\left( -\frac{x^2}{r_{th}^2(t)} - \frac{y^2}{z_{th}^2(t)} \right). \quad (2.38)$$

The time dependence of the condensate expansion is contained in  $\lambda_x$  and the time dependence of the thermal cloud expansion is in  $x_{th}$ . We fit the image to the above model with the parameters  $N_{tot}$  the total atom number,  $T/T_c$  the

reduced temperature, and cloud location.  $N_{tot}$  obtained from the fit gives  $T_c$ . Then reduced temperature gives  $T$  and the BEC fraction  $R = (1 - T/T_c)^3$ . The trap frequencies allow us to calculate the condensate and thermal cloud densities based on eqs. 2.32-2.35. Then we can determine the density of the unexpanded cloud at  $t = 0$ .

We made some changes to improve the imaging system. In the original design we used 25cm and 40cm regular achromats to image the cloud. The chamber design features special windows that enable us to place lenses very close to the atomic cloud for better resolution (see Fig. 2.3). We implemented new lens set up that can give close to diffraction limited performance ( $4.5\mu\text{m}$ ) in vertical direction and ( $8\mu\text{m}$ ) in the horizontal direction. The new lens set up was tested using a resolution target (Edmund Industrial Optics model R38-257). The lower resolution of the horizontal imaging setup is due the smaller window limiting NA.

### 2.4.3 Atomic Source

The atom source is a two chamber oven allowing us to load two distinct species into the chamber. The system is loaded with rubidium and bosonic lithium ( $^7\text{Li}$ ). Currently we are doing experiments with only  $^{87}\text{Rb}$  but the apparatus is equipped to trap lithium as well. Lithium setup is described in detail in the appendix. The drawing of the atom source is shown in Fig. 2.4. Lithium has much lower vapor pressure than rubidium. Thus, each chamber's temperature is controlled separately allowing us to load single species or both



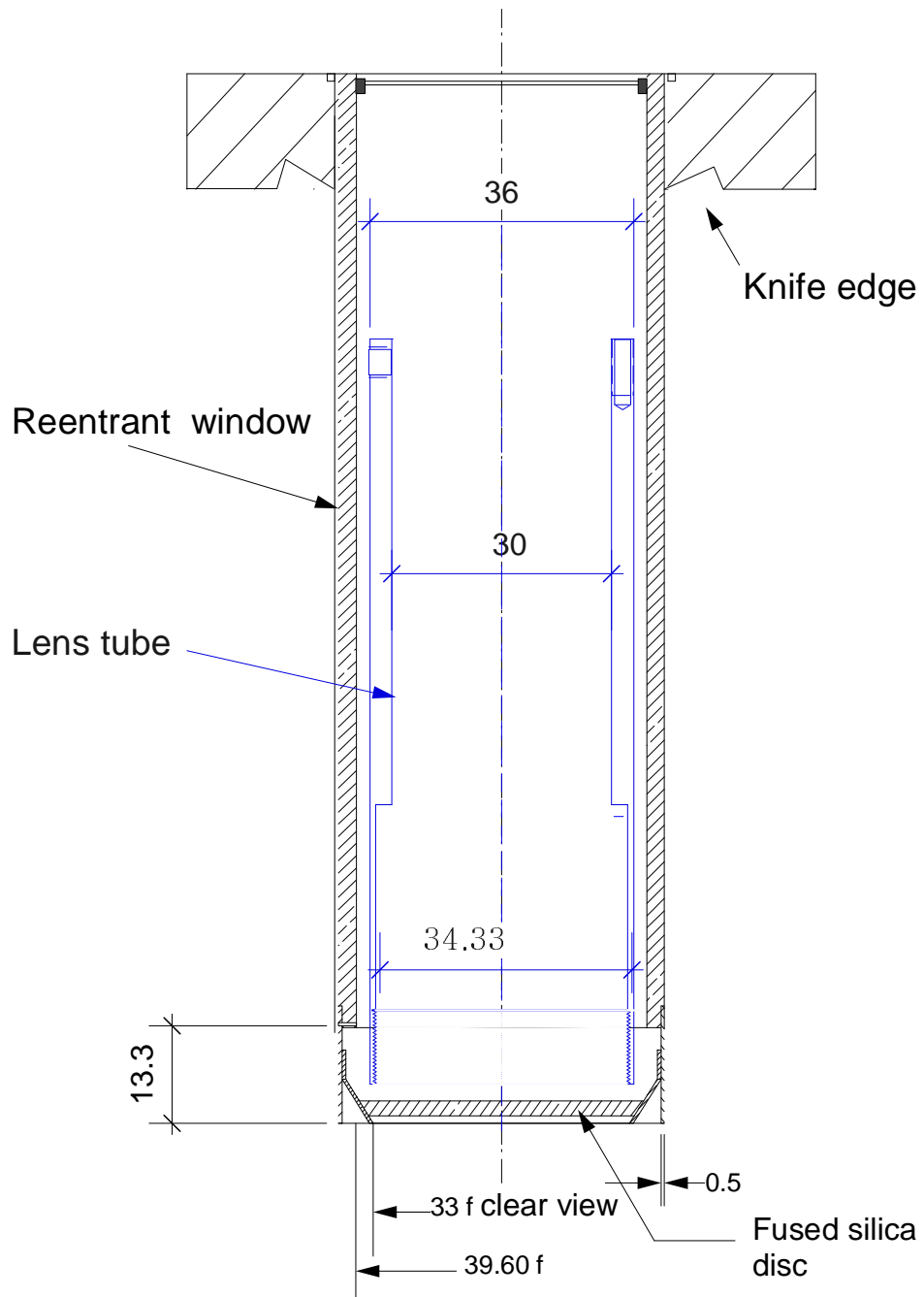


Figure 2.3: We can place the imaging optics very close to the atomic cloud by inserting the lens tube inside the re-entrant window. The dimensions are for vertical imaging.

species with comparable flux. The two species are mixed in the lithium chamber and form a single atomic beam to be slowed by the Zeeman slower. The lithium atoms can condense in the colder  $\approx 200^\circ\text{C}$  rubidium chamber. Thus the conductance of the main nozzle is about 50 times higher than the conductance of the rubidium nozzle to prevent lithium atoms condensing on the rubidium chamber (see Fig. 2.4). We only loaded  $\approx 3$  grams of lithium compared to the 25 grams of rubidium due the difference in mass ratio.

#### 2.4.4 Laser Set Up

The laser system for the  $^{87}\text{Rb}$  experiment consists of four different sources. Most of it is described in [51] and I will mention the set up briefly and describe the changes we made. A Coherent Verdi-10 pumps a Coherent MBR110 single frequency Ti:sapphire laser yielding an output of  $\approx 1.2\text{W}$ . This laser is locked close to F=2 transition using a lamb dip set up to supply the MOT, probe, slower and depopulator beams.

The original repumper laser required for the F=1 ground state to the F=2 excited state transition consisted of a 5 mW Master DBR laser (Yokogawa model:YL78XNW) and a 50 mw Slave utilizing injection locking. The master DBR laser failed and was replaced by the only spare we had. Unfortunately, the new DBR only lasted 16 days. With no DBR lasers for 780 nm in the market we decided to use a Littrow laser as our master laser. We had a spare Littrow housing originally built for lithium experiment. With minor modification we were able to use this housing with a 70 mw (model:DL7140-201) yielding an

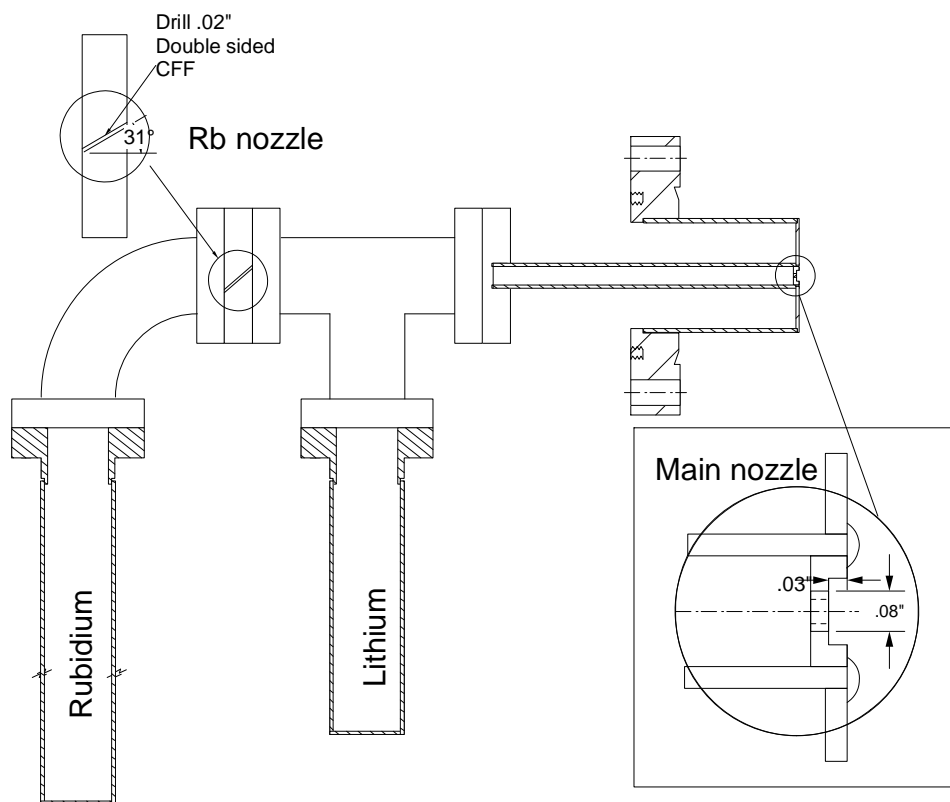


Figure 2.4: Drawing of the Rb/Li oven. The temperatures each chamber is controlled separately. For current experiment we use only rubidium by keeping the Rb chamber at 200°C, the Rb nozzle at 250°C, the Li chamber at 200°C, and the main nozzle at 250°C

output of 30 mW. We achieved a fiber coupling efficiency of  $\approx 60\%$  making the slave laser unnecessary. Mode hop free tuning range was only  $\approx 2$  GHz and the frequency of the laser drifted a few hundred MHz over a week that required us to readjust the angle of the grating in the system. We thought the frequency drift was due to temperature instability (5 mK) and added a secondary thermo-electric TE cooler and servo just underneath the laser diode housing. This improved the temperature stability to  $\approx 1$  mK. However, the laser frequency still drifted out of single mode operation over a week. This prompted us to try a lower power 30 mW diode (Sharp model:LT025MDO). This gave us a mode hop free tuning range of  $\approx 5$  GHz and long term stability. We think the better performance is due the difference in the power of the two diodes. If the diode is not AR coated then the lower power diodes work better than the higher power ones. The master laser has an output of  $\approx 15$  mW so we injection locked the slave to get 35 mW of power before fiber coupling.

The optical lattice beams are supplied by a Ti-Sapphire laser (Coherent 899-01) which is pumped by an Argon Ion laser. The optical lattice setup is described in ref. [51]. The output of this laser is passed through an AOM and the 1st order beam is delivered to the experiment table through a fiber. The intensity of this laser is stabilized by feedback using a pickup window after the output of the fiber. The laser is then split into three parts using two additional AOMs with center frequencies of 200 MHz and 40 MHz to provide the three sets of counter propagating beams for the lattice. The different frequencies are necessary to avoid interference between different lattice beams. Each of

these beams is then delivered into the chamber after being spatially filtered by fibers. Each beam is retro-reflected to form three sets of standing waves. The waist of the radial beams are set to  $260\ \mu\text{m}$  and that of the axial to  $130\ \mu\text{m}$ .

The Bragg spectroscopy and photoassociation (PA) experiment beams are supplied by a Ti-Sapphire laser (Coherent 899-21) pumped by a Verdi (Coherent V10). The main beam is split into two by a polarizing beam splitter. This way we send most of the power to the PA setup [51] and the rest to the Bragg setup (see Fig. 2.5). The Bragg beams consists of two parallel polarized beams delivered to the chamber with fibers. The angle between the two beams is  $\approx 28$  degrees and both are in the axial plane of the experiment. The RF sources for the two AOMs are phase locked to each other and we can have a very small frequency difference between the two Bragg beams. The Bragg beams have a beam waist of  $\approx 500\ \mu\text{m}$ . The fiber output couplers sending the beam into the chamber are on 2D translation stages allowing precise alignment of the beams onto the atomic cloud.

#### **2.4.5 Cooling Water**

The Argon Ion laser pumping the Ti-Sapphire for lattice laser and the magnetic trap coils dissipate more than 40 kW of power and need to be water cooled. The magnetic field of the trap is very sensitive to the chilled water temperature. The original servo on the chilled water system to control the temperature consisted of a proportional only gain controller (Johnson Controls

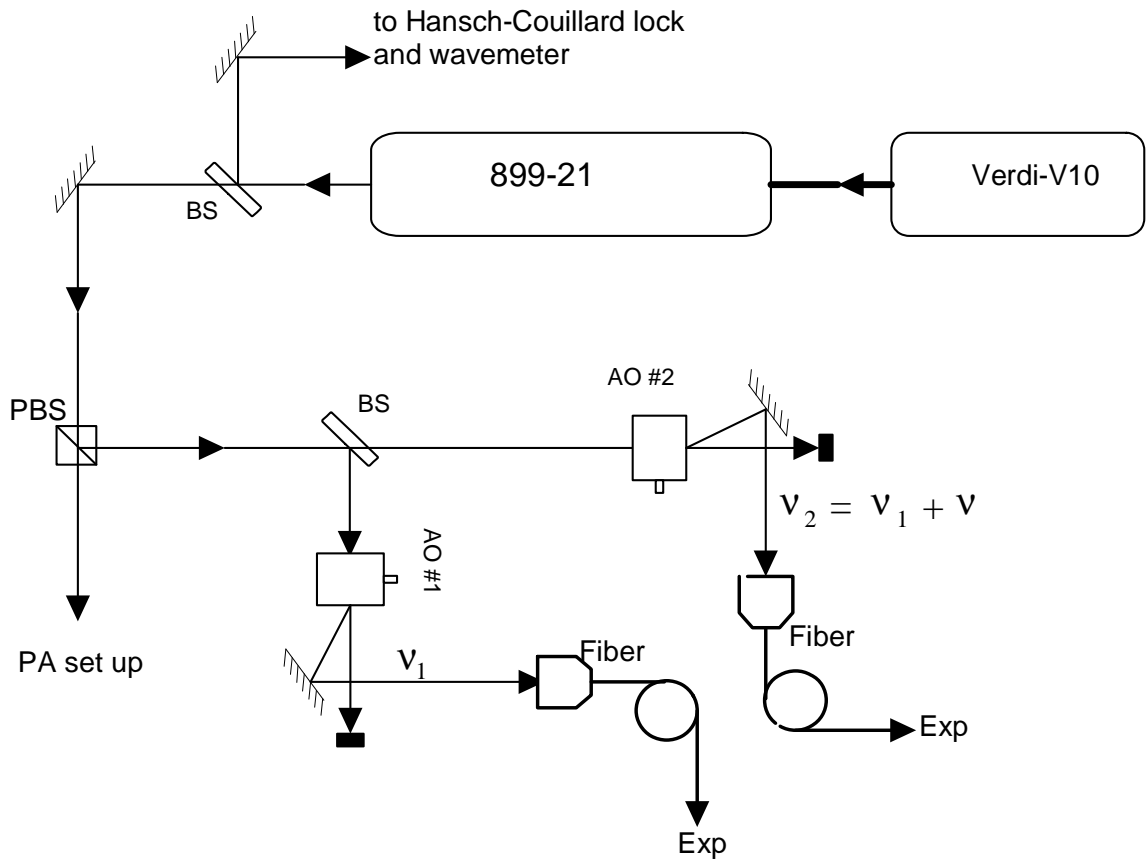


Figure 2.5: Bragg spectroscopy and photoassociation beams are derived from the same source. A polarizing beam splitter controls the amount of power going into each set up. The main Bragg beam is split into two and each beam passes through an identical AOM with a center frequency of 115 MHz. The frequency difference  $\nu$  between the beams is adjusted by changing the frequency of one of the AOMs. The beams are sent into the experiment chamber by fibers.

model:T-5800-1) that received a pneumatic signal from an immersion temperature sensor and put out a pneumatic signal to an 8" pneumatic valve (Siemens model 59901050) at the drain. The problem with this control was that whenever the main chilled water input parameters such as pressure changed the temperature of the water drifted causing big number fluctuations in the BEC. Thus, we installed a an electronic proportional and integral gain controller (Siemens model RWC62) that is input by a nickel temperature sensor (Siemens model 556-541). The output of the controller goes to a current/pressure transmitter (Moore Industries model IPT/4-20mA/3-27PSIG/35PSI) that converts the electronic signal into pneumatic signal to control the pneumatic valve. The new servo provided  $\approx .1^\circ\text{C}$  stability in cooling temperature measurement reducing the number fluctuations to  $\approx 10\%$ .

## 2.5 Measurement of the Excitation Spectrum in Optical Lattices

We create a BEC in a cloverleaf trap and load it into a 3D optical lattice. The BEC production and optical lattice setup are described in detail in [51] and I report here only the relevant parameters of the experiment. The magnetic trap is cylindrically symmetric with frequencies of 11.6 Hz and 20 Hz in the axial and radial direction respectively. The axial optical lattice beam has a beam waist around  $130\ \mu\text{m}$  and is aligned along the axis of the BEC. The radial lattice beams are orthogonal to each other and the axial lattice beam forming a simple cubic lattice. The radial beams each have a waist of 260

$\mu\text{m}$  and are both at 45 degrees to the horizontal as depicted in Fig. 2.6. The Bragg beams have a beam waist of  $500 \mu\text{m}$  each and are in the axial-horizontal plane with an angle of 28 degrees between them such that the difference wave vector  $q$  is directed radially (see Fig. 2.1). They are derived from the same source as explained in sect. 2.5.2 and are detuned 430GHz red from the  $^{87}\text{Rb}$  D1 line. The experimental procedure is as follows: After a BEC of about .5 million atoms are produced the lattice is quadratically ramped to a variable height  $V_0$  over 50 ms. Bragg beams are pulsed for 1ms with an intensity of around  $75 \text{ mW/cm}^2$  each yielding a two-photon Rabi frequency  $\Omega_{2p}$  of .25 kHz. Immediately after the Bragg pulse the lattice and the magnetic trap are turned off abruptly and the cloud is allowed to expand for 35 ms during which the quasi-particles are turned into free particles before we take a TOF image of the cloud from the vertical direction. The frequency difference between the two Bragg beams is varied and the experiment is repeated. The out-coupled atoms due to Bragg scattering are spatially separated from the unscattered atoms as seen in (Fig. 2.7). Thus, we call this measurement the out-coupling method. The scattering efficiency can be determined by comparing the number of atoms in the scattered cloud to the number in the unscattered cloud. The out-coupling method works well for low lattice heights. However, as the lattice is ramped up higher the expansion of the cloud becomes too large and the scattered atoms cannot be distinguished from the unscattered atoms. The larger expansion is probably due to due to the quantum depletion giving a bigger momentum distribution of the ground state of a single lattice site. Thus,



we use the out-coupling method just to measure the response of the BEC to Bragg beams for lattice strengths  $V_0 < 3.5E_r$ . We adopted a temperature measurement to detect the resonant response to the Bragg pulse for higher lattice strength. The experimental procedure is the same as the out-coupling method up to the pulsing of the Bragg beams. Then we quadratically ramp down the lattice to zero height in 20 ms. We wait about 5 ms to let the cloud come to thermal equilibrium before turning off the magnetic trap abruptly. After we turn off the magnetic trap the cloud is allowed to expand for 24ms after which we take a TOF image of the cloud from the horizontal direction. The image is fit as described in section 2.4.2, and the temperature and the BEC fraction of the cloud is determined from the fit. The excitations created during Bragg pulse will be damped into the system as heat and this will show up as an increase in the temperature of the system and a decrease in the condensate fraction. We changed the power of the Bragg pulses to verify that we are in the linear response regime. Note that the momentum transfer is fixed by the angle between the two Bragg beams and we find the resonant frequency  $\omega(q)$  for a single  $q$  for different lattice heights. The momentum transfer along the radial direction is  $q = .48k$  in a direction perpendicular to the trap symmetry axis. As we ramp up the lattice the momentum wave vector becomes smaller than the healing length putting us in the linear regime. We fit each scan of  $\omega(q)$  for a given lattice height to a Gaussian peak and the center of the peak gives the resonance frequency as shown in Fig. 2.8. We also use the temperature measurement for low lattice heights and verify that they agree

with the out-coupling method. If the Bragg beam power is increased beyond linear response we can see 2nd order effects. The atoms get a momentum kick of  $2q$  at a frequency difference of  $2\omega_0$  between the Bragg beams where  $\omega_0$  is the resonant frequency in linear response. This is observed both with the out-coupling method for low lattice heights as well as with temperature measurement. The resonant frequency is plotted for different lattice heights in Fig. 2.9. The Bogoliubov theory and the LDA (eq. 2.8) give a resonant frequency of  $\omega/2\pi = 850\text{Hz}$  for zero lattice strength. Our measured value is  $870 \pm 100\text{ Hz}$  with the error coming mainly from the atom number fluctuations. As we increase the lattice height the resonance frequency increases slightly up to  $V_0 = 2E_r$ . This is probably due to the faster increase of interaction energy  $U$  compared to the increase in effective mass  $m^*$ . The calculation of  $U$  is detailed in section 3.3.1. Here we just report that in the tight binding approximation ( $V_0 \gg E_r$ ) it scales as

$$U \propto \left(\frac{V_0}{E_r}\right)^{3/4}. \quad (2.39)$$

Thus,  $U$  increases with increasing lattice strength. The effective mass increases exponentially with lattice strength and from eqns. 2.20 and 2.21, scales as

$$\frac{m^*}{m} \propto \exp\left(2\sqrt{\frac{V_0}{E_r}}\right) \quad (2.40)$$

for  $V_0 \gg E_r$ . Thus, for strong lattice strength where tight binding approximation is valid the speed of sound decreases as

$$c \propto \exp\left(-\sqrt{\frac{V_0}{E_r}}\right). \quad (2.41)$$

For  $V_0 > 2E_r$  the resonance frequency decreases gradually. We attribute this to the decrease in the speed of sound due to the exponential increase of effective mass. The calculation of  $U$  and  $m^*$  for low lattice strengths need to be done numerically. As we are in linear regime the Bogoliubov speed of sound is readily obtained through  $c = \omega_0/q$  from our data. The error is smaller in the estimation of  $c$  for stronger lattice. Thus, we compare our data for the strongest lattice where we can still see superfluid excitations in the linear regime. From eq. 2.41 and using the linear phonon regime our excitation energy should decrease by a factor of  $\exp(-\sqrt{\frac{V_0}{E_r}})$ . For zero lattice strength the resonant excitation energy is 870 Hz and for lattice strength  $V_0 = 9.8E_r$  tight binding approximation gives a resonant excitation frequency of  $\omega_0/2\pi=380$  Hz. We measure  $\omega_0/2\pi=420$  Hz. The uncertainty in our measurement is  $\approx 120$  Hz coming mainly due to the uncertainty in the calibration of lattice strength as explained in section 3.3.2. This shows our measurement is in agreement with the phonon excitations of superfluid. Observation of sound modes in the BEC in optical lattice is independent proof of the coherence of the superfluid throughout the lattice. Our data may provide theorists with valuable information as we try to understand the strongly interacting superfluids better.

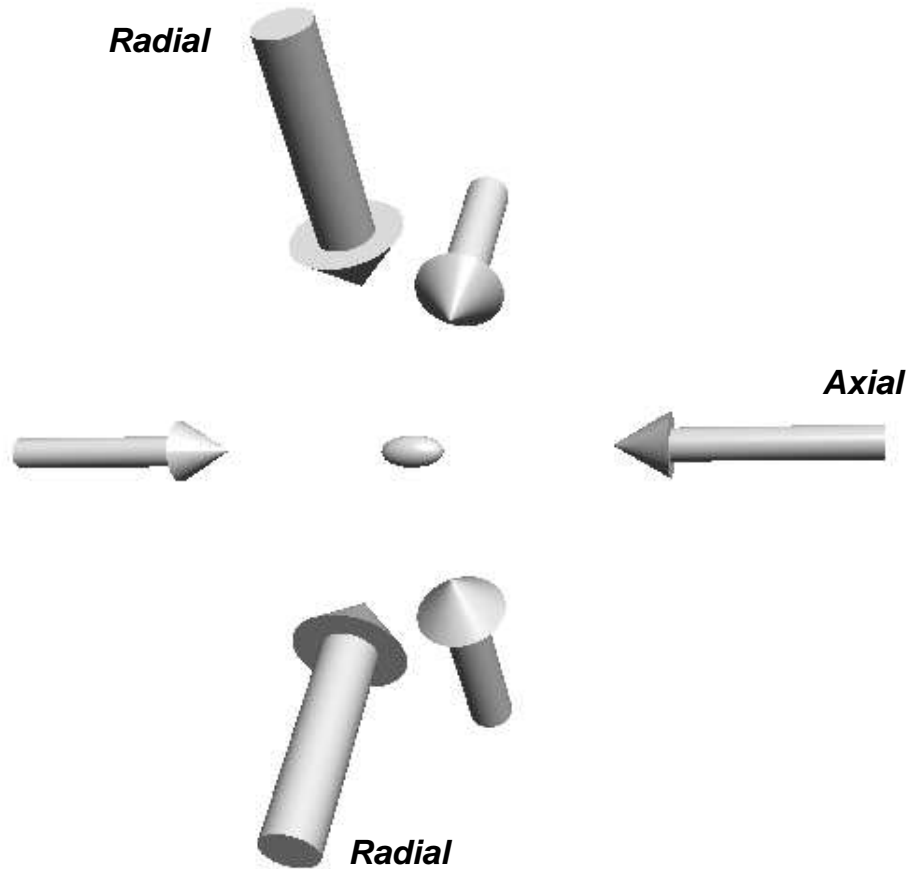


Figure 2.6: 3-D optical lattice set up. Two radial direction optical lattice beams are 45 degrees to vertical and horizontal directions. Imaging direction is horizontal or vertical which will be 45 degrees to radial direction optical lattice beams.

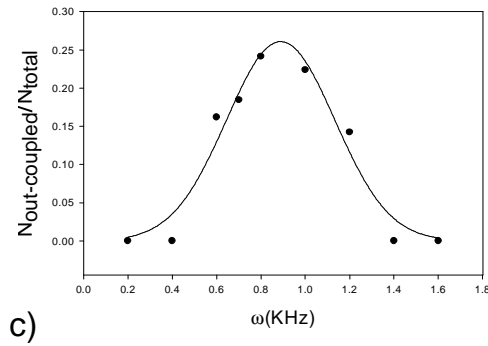
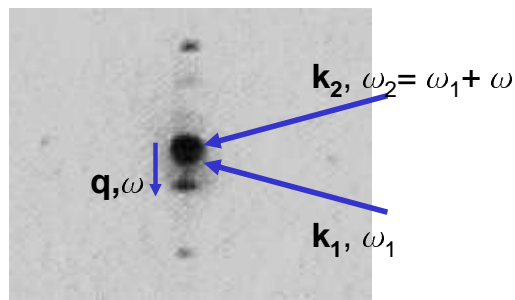
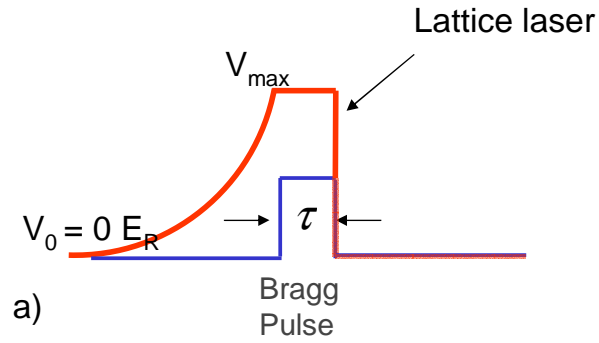


Figure 2.7: Bragg Scattering in Optical Lattice. a) Lattice and Bragg laser beam intensities as a function of time. The lattice laser is quadratically ramped up over 50ms and then the Bragg pulse is applied for 1ms, after which both beams are suddenly turned off along with magnetic trap. b) Time-of-flight (TOF) image taken after 35ms of free expansion. The scattered atoms are spatially separated from the unscattered cloud. c) Ratio of scattered atoms to the unscattered atoms for  $V_0 \approx 2E_r$  for different  $\omega$ .

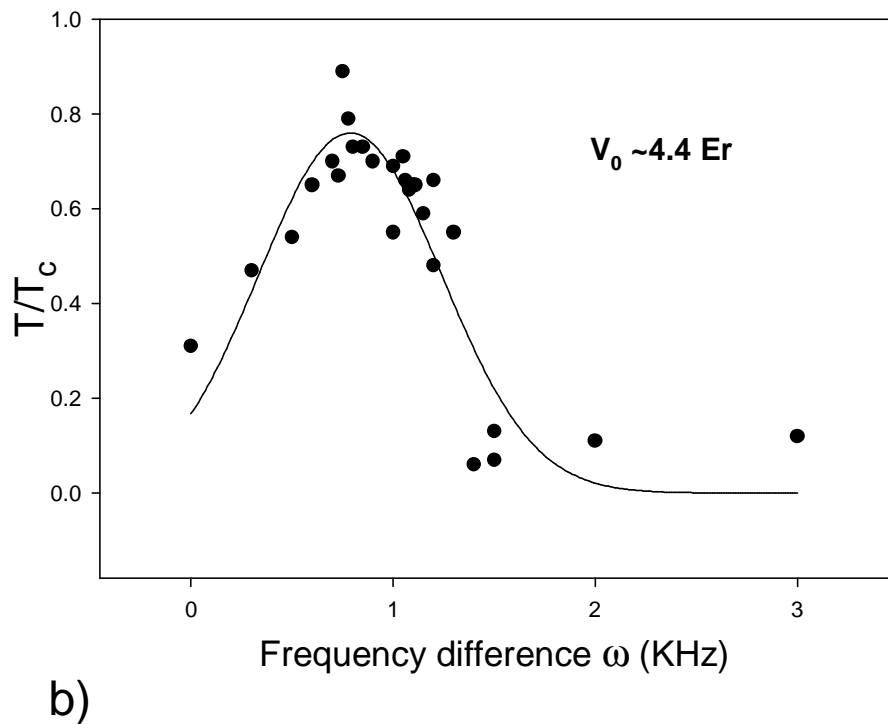
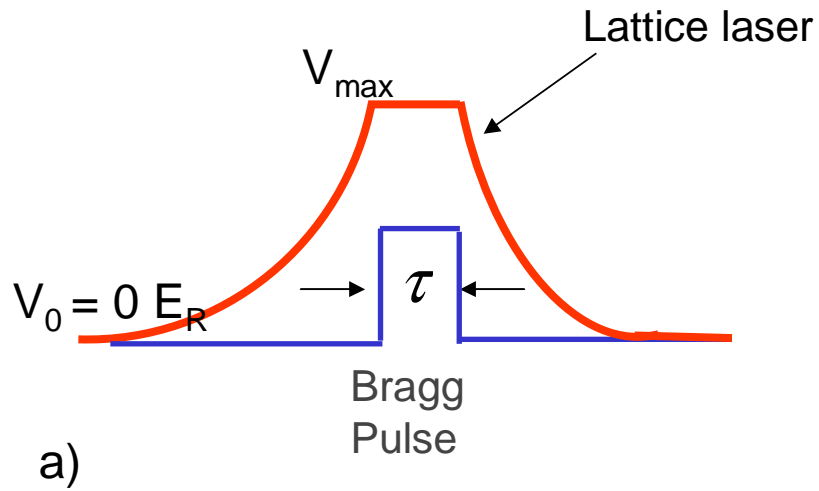


Figure 2.8: a) The schematic of the lattice and Bragg lasers are shown. The lattice is ramped up quadratically over 50ms. The Bragg pulse duration is 1ms and the lattice is ramped back down in 20ms. b) The resonant excitations during the Bragg pulse are damped into the system as heat. The response is fit to a Gaussian and the center is taken as the resonance frequency.

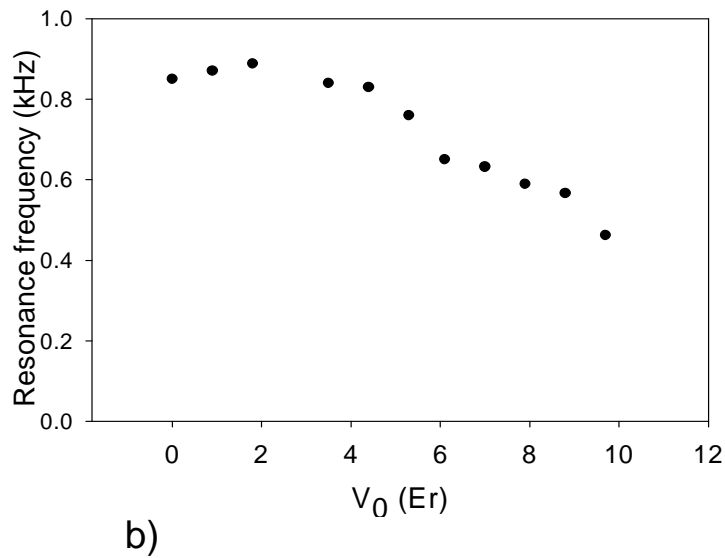
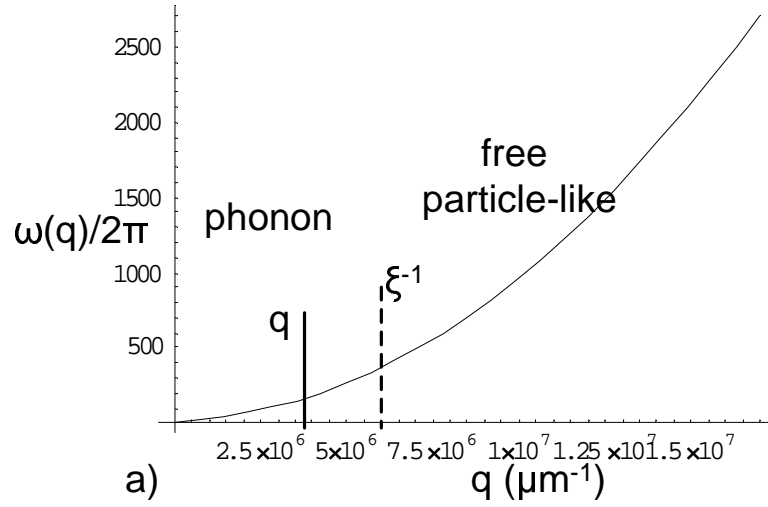


Figure 2.9: a) Dispersion relation showing the phonon (linear) regime for  $q < \xi^{-1}$  and free particle-like regime for  $q > \xi^{-1}$ . In the experiment  $q = 3.8 \times 10^6 \mu\text{m}^{-1}$  and  $\xi^{-1} \approx 6.5 \times 10^6 \mu\text{m}^{-1}$ . b) The resonance frequency as a function of lattice height. Since we are in the linear regime the speed of sound is readily obtained through  $c = \omega(q)/q$ . The speed of sound  $c = \sqrt{\frac{U}{m^*}}$ . The decrease in excitation frequency for  $V_0 > 4E_r$  is due to the decrease in  $c$ .

## Chapter 3

### Mott Insulator

The Mott insulator phase is the state when atoms are localized to individual lattice sites due to repulsive interactions between them. These repulsive interactions increase with increasing lattice height. For low lattice heights the system is a superfluid and atoms are spread throughout the lattice as would be expected from a BEC. In the superfluid state the atoms can move freely through the lattice. A condensate exhibits coherent wavelike behavior which can be observed with interference just like the interference of coherent laser light. In the Mott insulator state because the particles are localized to individual lattice sites, they do not have phase coherence and would not exhibit any interference. The loss of coherence can be probed in time-of-flight (TOF) images and this method has been used to demonstrate the transition to the Mott insulator phase [28]. However, the loss of coherence alone is not proof of the Mott insulator phase because processes such as heating during the loading of the BEC to the lattice can cause loss of coherence. Also, phase coherence does not go to zero close to the transition in the Mott insulator state. Another feature of the Mott insulator phase is a gap in its excitation spectrum. The lowest lying excitations for such a state are particle-hole excitations. In our system this corresponds to an addition of an atom to one lattice site



and removal of an atom from another lattice site as shown in Fig. 3.5. In the superfluid there is no certainty in the number of atoms per site so such excitations can be activated at all energies. However, in the Mott insulator state the addition of an atom to a lattice site from another lattice site, i.e hopping of one atom from one site to another, costs an energy that determines the gap in the excitation spectrum. In the original experiment by Greiner et al. [28] this gap was detected by tilting the lattice. Another group shook the lattice in one direction to create excitations by putting sidebands to the lattice [29]. However, for the latter experiment, there should be no scattering in linear response and the response is probably due to nonlinear effects [30, 52]. Both experiments show similar data with a discrete excitation spectrum, but do not provide any means to observe the opening of the gap that characterizes the insulator state. We use Bragg spectroscopy in linear response to measure the particle-hole excitations and observe the opening of the excitation gap in the transition from the superfluid to the Mott insulator phase.

### **3.1 Quantum phase transition from a Bose-Hubbard model**

Jaksch et al. [27] showed that ultra-cold atoms in optical lattices is a perfect realization of the Bose-Hubbard model originally studied by Fisher [26]. This model predicts a phase transition from a superfluid to a Mott insulator state. To show that ultra-cold atoms in optical lattices can be described by the Bose-Hubbard model Jaksch et. al. started with the Hamiltonian for bosons

in an external trap [27]

$$H = \int d^3x \psi^\dagger(x) \left( -\frac{\hbar^2}{2m} \nabla^2 + V_0(x) + V_T(x) \right) \psi(x) + \frac{1}{2} \frac{4\pi a_s \hbar^2}{m} \int d^3x \psi^\dagger(x) \psi^\dagger(x) \psi(x) \psi(x) \quad (3.1)$$

where  $\psi(x)$  is the boson field operator for the atoms in the optical lattice,  $V_0(x)$  is the optical lattice potential and  $V_T(x)$  is an external trapping potential (magnetic trap in our case). In sec. 2.3.2 we stated that the eigenstates of a system in a periodic structure are Bloch functions. As the lattice potential is ramped up the atoms become localized to individual lattice sites. The Bloch states are not localized eigenstates but a superposition of such states gives the Wannier functions which are localized and can be used to describe the atoms in the lattice. The wave function can be written as

$$\psi(x) = \sum_i b_i w(x - x_i) \quad (3.2)$$

where  $b_i$  is the annihilation operator and  $w(x - x_i)$  is the Wannier function for  $i^{\text{th}}$  lattice site. For this expression only the lowest vibrational state is included. This is justified by the fact that the energy needed to excite the second band is a lot higher than the energies involved in the system. If we substitute eq. (3.3) into eq. (3.2) the Hamiltonian can be rewritten as

$$H = -J \sum_{\langle i,j \rangle} b_i^\dagger b_j + \sum_i \epsilon_i n_i + \frac{1}{2} U \sum_i n_i (n_i - 1) \quad (3.3)$$

where the operator  $n_i$  gives the number of atoms in site  $i$ ; the parameter  $J = \int d^3x w^*(x - x_i) [-\frac{\hbar^2}{2m} \nabla^2 + V_0(x)] w(x - x_j)$  is the hopping matrix element between adjacent sites,  $U = \frac{4\pi a_s \hbar^2}{m} \int d^3x |w(x)|^4$  corresponds to the on site interaction energy between atoms and  $\epsilon_i = \int d^3x V_T(x) |w(x - x_i)|^2$  is the energy offset of each lattice site. This term is due to the inhomogeneity of the trap. It is zero at the center of the trap and equals to the chemical potential at the edge. Now, the Hamiltonian takes the form of a Bose-Hubbard model.

The Wannier functions can be approximated by a Gaussian ground state wave function corresponding to the harmonic trap of a lattice site for  $V_0 \gg E_r$ . This results in analytic expressions for  $U$  (eq. 3.8) and  $J$  (eq. 2.18).

Fischer studied the Bose-Hubbard model and constructed a phase diagram [26]. Much insight can be gained by studying this diagram plotted in (Fig. 3.1).

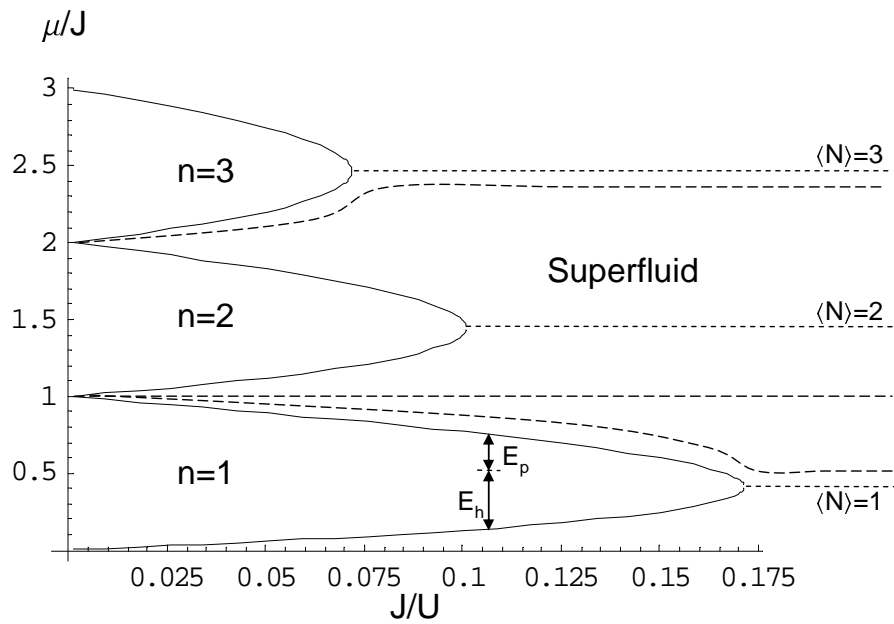


Figure 3.1: Chemical potential as a function of  $J$ . Increasing lattice strength corresponds to decreasing  $J/U$ . The system is superfluid for  $J/U \gg 1$ . The particle and hole excitation energies are shown for a point in the one atom per site Mott insulator region. This plot was generated in Mathematica using the result of [53] obtained by minimizing the variational energy per site.

Let us consider the limiting case of  $J = 0$ . The on site energy will be given by from the Bose-Hubbard Hamiltonian (eq. 3.3) [26]

$$\epsilon(n) = -\mu n + \frac{1}{2}Un(n-1). \quad (3.4)$$

Each lattice will be filled with the same integer number ( $n$ ) of atoms that minimizes this energy. From Fig. 3.1 it can be seen that for  $n - 1 < \mu/U < n$  exactly  $n$  bosons occupy each lattice site. If we start increasing  $J$  by decreasing the lattice height, the atoms will gain kinetic energy if they can hop to other lattice sites. However, the atoms cannot hop until the kinetic energy gained from such a process is on the order of the on site interaction energy  $U$ . Thus, for large lattice heights when  $J/U \ll 1$  the atoms cannot hop around and form regions where each lattice site is occupied by a fixed number of atoms. These constant  $n$  regions are incompressible and form Mott insulating phases. The atoms are completely localized to individual lattice sites. This means the atom number on each lattice site is determined which gives a vanishing expectation value for  $b_i$ . This translates into no phase coherence between lattice sites. Once  $J$  is big enough to overcome the repulsion on the lattice sites the particles can hop around and form a superfluid.

There have been experiments with two dimensional systems such as  $^4He$  films [54] and flux lines in superconductors with artificial pinning centers [55] that attribute observed experimental effects to the formation of Mott insulating regions. There has also been an experimental study with a one dimensional system of Josephson junction arrays [56] to study the Bose-Hubbard

phase diagram along with numerous theoretical calculations [57–59].

It should be noted that this transition is a quantum phase transition because it is due to the competition between terms in the ground state energy of the system, as opposed to the terms in the free energy [60]. Thus, the transition can occur even at zero temperature.

### 3.1.1 Probing Phase Transition with Momentum Distribution

When we take a time of flight (TOF) image we look at the momentum distribution of the cloud. Neglecting interactions between the atoms during the expansion, the momentum distribution is the Fourier transform of the spatial distribution in the trap. When a BEC in the lattice is allowed to expand by suddenly turning off all the confining potential (magnetic trap and the lattice potential) the wave-packets confined to individual lattice sites expand and overlap with each other. Due to the phase coherence over the whole lattice we observe the interference of the wave-packets or matter waves from different lattice sites. The momentum distribution in the lattice can be expressed as [40]

$$n(\mathbf{k}) = n|w(\mathbf{k})|^2 \sum_{\mathbf{R}} e^{i\mathbf{k}\cdot\mathbf{R}} \rho_1(\mathbf{R}) \quad (3.5)$$

where  $\rho_1(\mathbf{R}) = \langle b_{\mathbf{R}}^\dagger b \rangle$  is the one particle density matrix at separation  $\mathbf{R}$  with  $b_i^\dagger$  the particle creation operator at site  $i$ .  $(\mathbf{k})$  is the Fourier transform of Wannier function. The summation is over all the lattice vectors  $\mathbf{R}$  which are integer multiples of the primitive lattice vectors. Zwerger [40] pointed out that

in the superfluid for large  $\mathbf{R}$  the one particle density matrix approaches a finite value and  $n(\mathbf{k})$  has a peak proportional to the total number of particles at the reciprocal lattice vectors  $\mathbf{k}$  defined by  $\mathbf{k}\cdot\mathbf{R} = 2\pi$ . These interference peaks can be seen in Fig. 3.2. The width of the interference peaks is the Fourier transform of the ground state wave function size. For the superfluid the ground state wave function extends over the whole lattice and there is no broadening of the momentum peaks. In the Mott insulator phase however,  $\rho_1(\mathbf{R})$  goes to zero and the momentum peaks no longer scale with the total atom number. Close to the transition in the Mott insulator interference peaks are still present as long as  $\rho_1(\mathbf{R})$  extends over a few lattice sites. Deep in the Mott insulator state the phase coherence is lost completely and the momentum distribution becomes a Gaussian with no peaks. In real experiments the momentum peaks are broadened due to interactions between the atoms during the expansion but still provide a lower bound for the coherence length in the system.

We use such TOF images to measure the width of the momentum peaks to observe the phase transition from the superfluid to the Mott insulator. To do the experiment we load a BEC of  $^{87}\text{Rb}$  in a 3D optical lattice which is quadratically ramped up over 50ms to a height  $V_0$ . We then turn off the magnetic trap and optical lattice suddenly and allow the atomic cloud to expand for 20 ms and take an image. We start from zero lattice height and repeat the experiment for lattice heights up to  $V_0 = 20E_r$ . The TOF images are shown in Fig. 3.2. The radial side peaks are in the vertical direction and axial side peaks are in the horizontal direction. Each of these peaks is  $2\hbar k$  from

the central peak due to the periodicity of the lattice. The fact that the radial peaks look closer is due to the imaging direction which is  $45^\circ$  to the radial lattice beams directions. Radial and axial cross sections were fit by Gaussian functions as shown in Fig. 3.3. We plot the central peak width as a function of the lattice height in Fig. 3.4. The interference peaks initially grow with increasing depth of lattice. This is due to the fact that the Wannier functions in eq. 3.6 become more localized giving a larger Fourier transform. The width of the peaks however, remain constant up to a certain lattice height. The width of the interference peaks start broadening for  $V_0 \geq 13E_r$  which we interpret as the signature of the quantum phase transition. Stoferle *et al.* have observed similar results where they saw a sudden broadening of the interference peaks [61] which they interpret as the onset of the superfluid-insulator transition. Kollath *et al.* studied one-dimensional bosons in optical lattices [62]. They conclude that the sudden broadening of the interference peak is due the decrease in correlation length when the insulator state forms. The correlation length is inversely proportional to the width of the interference peak and diverges for the superfluid being equal to the size of the system. The correlation length become finite in the Mott insulator due to the opening of an excitation gap. The situation is different for an inhomogeneous system where the co-existence of the superfluid and insulator prevents a sudden increase of the interference peak width, as shown by calculations on the inhomogeneous system. We conclude that even though the sudden broadening of the peak width is due to Mott insulator, the existence of the superfluid close to the



transition may delay this broadening, i.e the peak width may still show no broadening till the superfluid fraction becomes negligible. The occupation numbers for Bloch states with quasi-momentum  $k$  are proportional to the intensity of the interference peaks [63]. The intensity of the central peak is proportional to the population of the  $k=0$  Bloch state or the number of atoms in the condensate. The emergence of a broad background is attributed to the quantum depletion of the condensate as the interactions between the atoms are increased. The increased interactions for stronger lattice transfers atoms from the  $k=0$  state to higher quasi-momenta states which translates to the broad background in the TOF images. The broadening of the interference starts around  $13E_r$  which is close to where we expect to see the phase transition. It was also argued that the interference images does not give direct information on the superfluid fraction in the system [63]. Thus, we can argue that the images can give a quantitative information on the quasi-momentum distribution of the system but not the superfluid fraction.

### 3.2 Excitations in the Mott Insulator

The lowest lying excitations in the Mott insulator region are the particle-hole excitations. In our system a particle (hole) excitation corresponds to an addition (removal) of one atom to (from) a lattice site. The energy required to create such an excitation is the minimum vertical distance in  $\mu$  for a fixed  $J$  from the upper (lower) phase boundary shown in Fig. 3.1. Suppose a lattice site is in a Mott insulating region with chemical potential  $\mu$  and  $U \gg J$  such

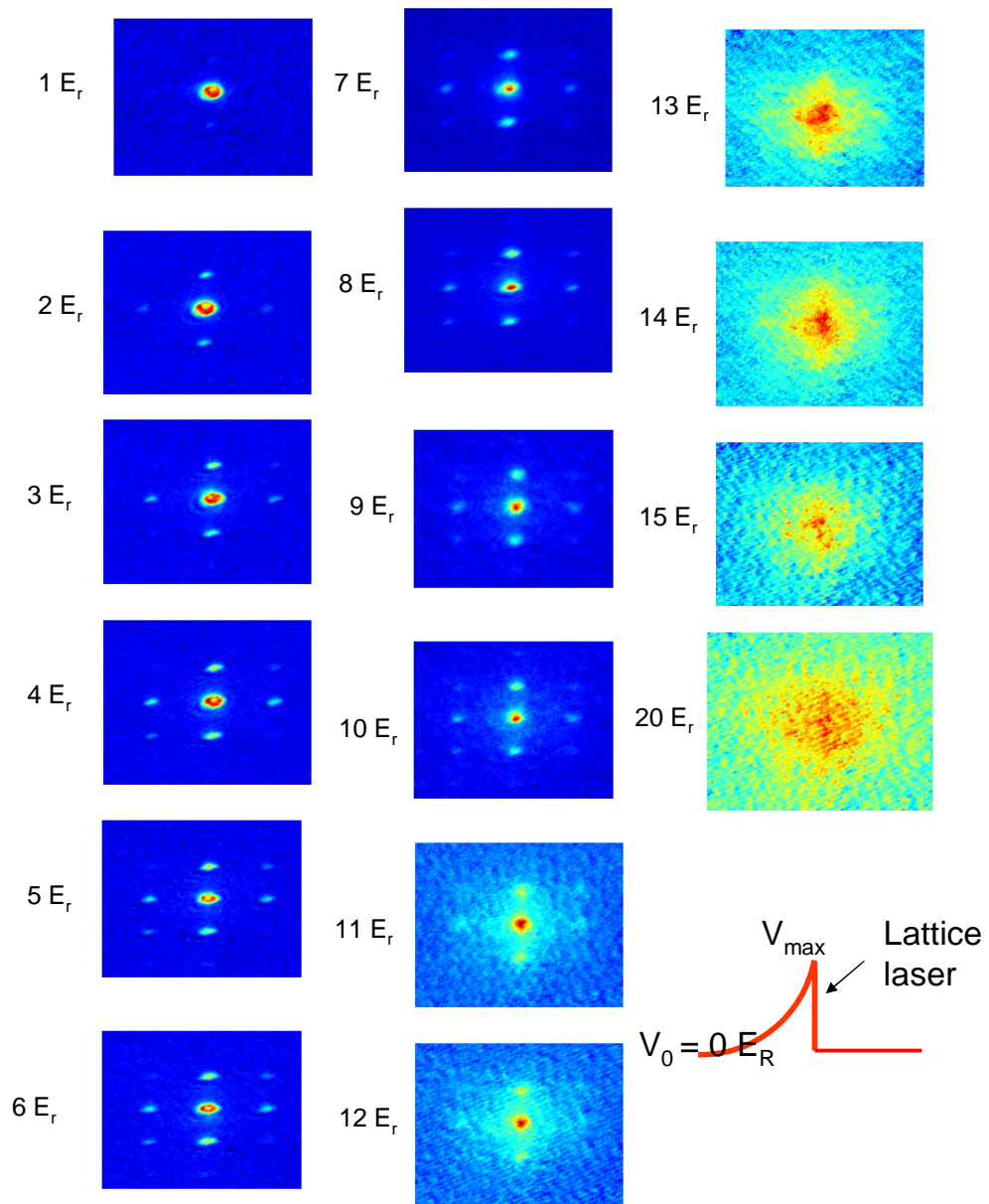


Figure 3.2: Matter wave interference peaks after 24ms TOF. After ramping the 3-D optical lattice depth up to the final depth, the magnetic trap and optical lattice beams were turned off suddenly.

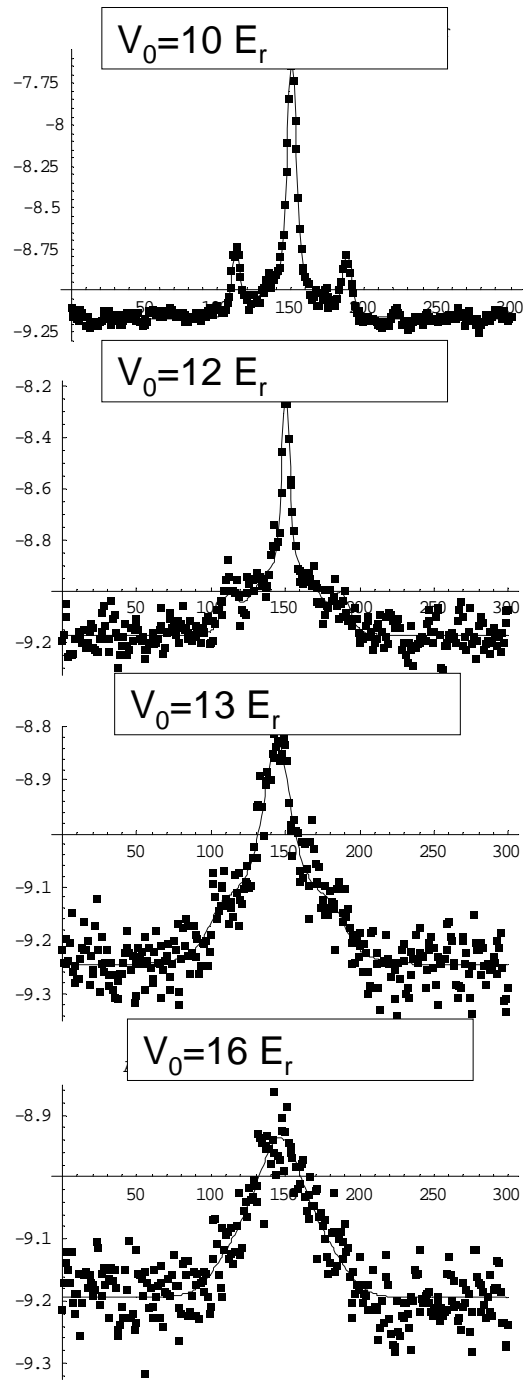


Figure 3.3: One pixel is  $6 \mu\text{m}$ . The peak width starts broadening for  $V_0 > 13E_r$ .

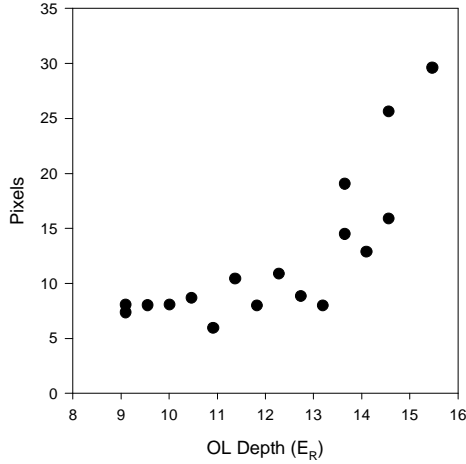


Figure 3.4: The central gaussian peak width as a function of lattice strength in recoil energy. The vertical axis unit is pixels where 1 pixel is  $2.4 \mu m$ .

that we can ignore  $J$ . Then the energy required to add an atom to that lattice site is [64]

$$E_p = -\mu + \frac{1}{2}U(n+1)n - \frac{1}{2}Un(n-1) = Un - \mu \quad (3.6)$$

and the energy required to remove an atom from that lattice site is

$$E_h = -\mu + \frac{1}{2}U(n-1)(n-2) - \frac{1}{2}Un(n-1) = U(n-1) - \mu. \quad (3.7)$$

However, in our system the atom number is conserved such that the lowest excitation is a particle and a hole excitation, i.e. an atom hops from one lattice site to another. The energy required for this particle and hole excitation known as the energy gap, is  $E_p + E_h \equiv E_{gap}$ . This is the difference in  $\mu$  between the upper and lower phase boundary in Fig. 3.1 and is equal to  $U$  for deep in the Mott insulator state where  $J$  is negligible. We can understand this by looking at Fig. 3.5. The on site interaction energy for two atoms in a lattice site is  $U$ .

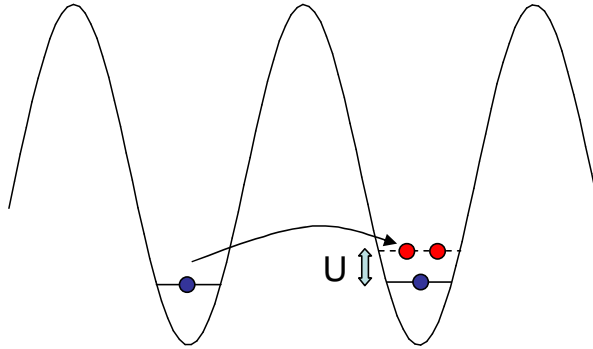


Figure 3.5: Initially each site is occupied by one atom. It costs an energy  $U$  equal to the on-site interaction energy for an atom to hop from one site to the other if they both have the same number of atoms.

Thus it costs an energy  $U$  for a particle to hop from one site into the other if both have the same number of particles. To understand why this gap is equal to the vertical distance from the upper to the lower phase boundary we can consider a hole at the lower boundary for a fixed  $J$ . Then if we want to add a particle it costs the same energy all the way to the top phase boundary since the mean occupation per site is the same inside the Mott lobe. Note that in the superfluid region (high  $J/U$ ) region in Fig. 3.1 the atom number in each site is undetermined. Thus, there is no energy gap for particle-hole excitations. Probing these excitations provides us with a unique method to detect the quantum phase transition from the superfluid to the insulator state as the latter state will have a gap in its excitation spectrum. The critical value of  $U/J$  at which this transition occurs is  $(U/J)_c = 5.8z$  where  $z$  is the number of nearest neighbors [26, 65, 66]. For a 3D lattice  $z$  is 6. Scaling theory [26] predicts the opening of the gap to be of the form

$$E_g \propto ((U/J) - (U/J)_c)^\alpha \quad (3.8)$$

with mean field calculations giving  $\alpha = 1/2$ , hence the parabolic shape of the Mott lobes. If we can measure the particle hole excitations accurately we can not only observe the phase transition but also study the dynamics of the transition as well acquiring experimental insight into the phase diagram. This is the motivation behind performing Bragg spectroscopy of the Mott insulator. To understand what to expect from the experiment we should discuss the differences between the homogeneous and inhomogeneous cases.

A homogeneous system has a uniform average occupancy  $\langle n \rangle$  per site. If  $\langle n \rangle$  is an integer the system enters the Mott insulator state at the right tip of the Mott lobe (maximum  $J$  value at the phase boundary) as shown in Fig. 3.1. In the homogeneous system non integer occupancy contours always remain in the superfluid region joining the  $J = 0$  axis at  $\mu = n$  for  $\langle n \rangle > n$ . Likewise the density contours between  $J = 0$  axis at  $\mu = n - 1$  for  $\langle n \rangle < n$ . What this means is that the local chemical potential  $\mu_i$  changes to keep a constant occupancy  $\langle n \rangle$  since  $\langle n \rangle$  is fixed in the homogenous system. Thus, a homogeneous system with non integer filling per lattice site cannot cross into the insulator region.

The inhomogeneous case formed by an external trap as in our experiment gives a non-uniform filling over the lattice. local density approximation is employed to describe such a system. For this method the system is divided into several regions such that within each region the atom number change is

small so that each region can be treated as a homogeneous system. A local chemical potential for the  $i^{\text{th}}$  lattice site is defined as

$$\mu_i = \mu - \epsilon_i \tag{3.9}$$

where  $\epsilon_i$  is the energy offset at that site. Even though we have a locally homogeneous system, the fixed parameter is  $\mu_i$  instead of the density  $n$ , as  $J/U$  is increased the density can change and cross into the Mott insulator region. The inhomogeneous trap causes the chemical potential  $\mu_i$  for a lattice site close to the center of the trap to be different than the chemical potential for a lattice site away from the center as can be seen in Fig. 3.6. Going from the center to the edge of the trap local chemical potential decreases from the total chemical potential  $\mu$  to zero, spanning a vertical line (vertical black arrows in Fig. 3.6). Let us consider the case in which the center of the trap is in a Mott insulating state with two atoms per lattice site (Fig. 3.6c). As we go further out there will be a region of superfluid followed by a region of a Mott insulating phase with one atom per site and finally an outermost superfluid shell (Fig. 3.6).

As mentioned earlier the particle-hole excitations in the superfluid do not have an energy cost, thus if we transferred energy into the system we expect to see no gap in the excitations. As we cross into the insulator region from the superfluid region we expect to see a suppression of the particle-hole excitations of the superfluid. The excitations are not suppressed completely because in an inhomogeneous system there is always some superfluid present. For a given

initial number of atoms and chemical potential the volume of different states will be determined by the value of  $J/U$ . The superfluid fraction will be less as  $J/U$  goes to zero. Finally we should see particle-hole excitations of the Mott insulator if the energy transferred to the system can overcome the particle-hole energy gap  $E_g$ .



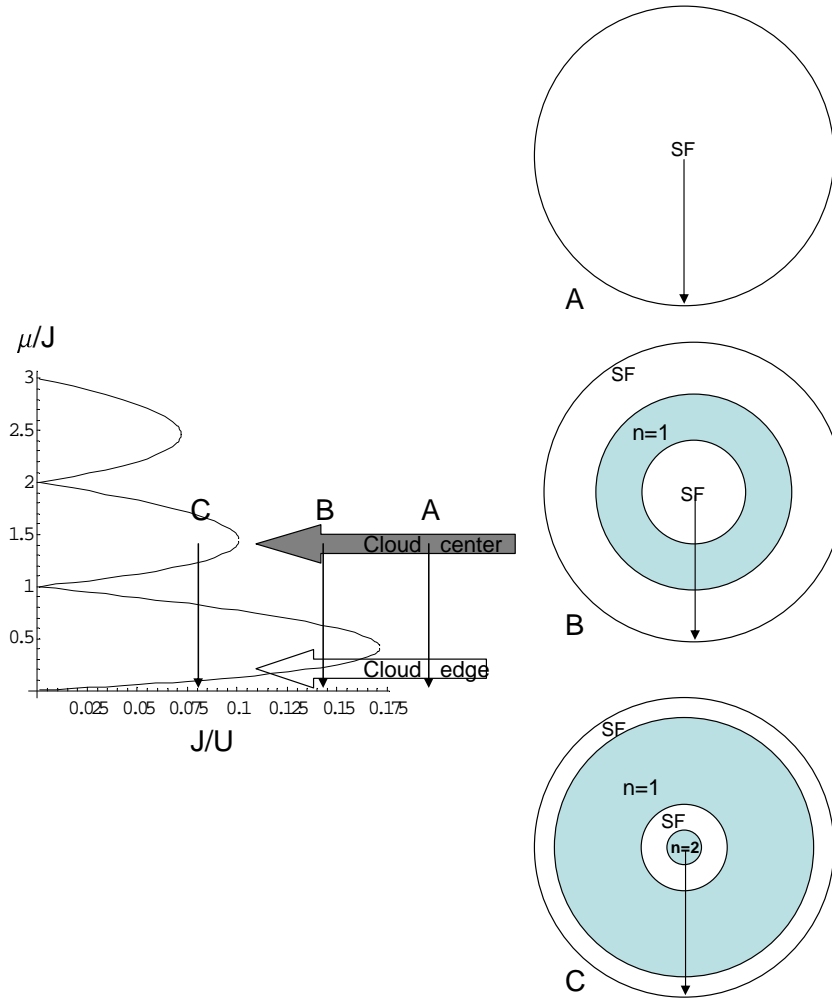


Figure 3.6: As we decrease  $J/U$  the system changes from a complete superfluid (A) to a coexistence of superfluid and Mott domains. This coexistence of superfluid and Mott insulator domains is due to the inhomogeneity of the system. The dark and light arrows represent the chemical potential of the center and edge of the cloud where the chemical potential decreases going from the center to the edge as indicated by the black vertical arrows. When the system first crosses into the Mott-insulating region only the middle of the cloud becomes an insulator while the center and edge remain superfluid (B). As  $J/U$  is decreased even further the center of the cloud forms a two atom per site Mott insulator, then there is a superfluid region followed by a one atom per site Mott insulator, and finally an outermost superfluid shell (C).

### 3.3 Preparing the Mott Insulator

#### 3.3.1 Loading Atoms into the Optical Lattice

The dynamics of the atomic cloud in the optical lattice needs to be examined to understand the path we are taking on the Bose-Hubbard phase diagram. As the lattice is ramped up there will be extra confinement from the lattice beams due to their Gaussian profile. This increases the trap frequency where the contribution from the lattice lasers is given by eq. 2.17. On the other hand the repulsive interactions between the atoms are increased because of this tighter confinement which tends to expand the cloud. A mean field approach can be taken to calculate the on site interaction  $U$  by considering each site as a separate condensate. Then the interaction  $U$  can be calculated by integrating the on site wave function over one lattice site such that there is a correction to the normal mean field interaction  $g$ :

$$U = g \int |\omega(x)|^4 \quad (3.10)$$

where  $\omega(x)$  is the Wannier function of the lowest band and the integration is over a volume of the unit cell. We can approximate the Wannier function by the oscillator ground state wave function of the individual lattice site. This approximation written in terms of the recoil energy  $E_r$  yields

$$U \approx 4\sqrt{2\pi} \frac{a_s}{\lambda} E_r \left( \frac{V_0}{E_r} \right)^{3/4} \quad (3.11)$$

where  $a_s$  is the s-wave scattering length. Even though this is only an approximation and is valid for  $V_0 \gg E_r$  it can be used to estimate the chemical potential for lattice heights close to the insulator transition. The new chemical potential is calculated for a Thomas Fermi shape using the new trap frequencies and the new  $U$  from eq 3.12. The increased  $U$  can be thought of as an increase in the  $g$  such that the new  $g$  is  $g^* = g \int |\omega(x)|^4$ . The Thomas Fermi density profile is

$$n_{TF}(r, z) = \frac{1}{U} \left( \mu - \frac{1}{2} m \omega_{rcom}^2 r^2 - \frac{1}{2} m \omega_{zcom}^2 z^2 \right) \quad (3.12)$$

and the Thomas Fermi radii are

$$r_{TF} = \sqrt{\frac{2\mu}{m\omega_{rtot}^2}}, z_{TF} = \sqrt{\frac{2\mu}{m\omega_{ztot}^2}} \quad (3.13)$$

where  $\omega_{rtot}$  and  $\omega_{ztot}$  are the combined trap frequencies due to the magnetic and the dipole trap, and can be calculated easily at a given lattice strength. The chemical potential can be expressed as

$$\mu = \left( \frac{15 NU \bar{\omega}^3 m^{3/2} (\lambda/2)^3}{16 \sqrt{2\pi}} \right) \quad (3.14)$$

with  $\bar{\omega}^3 = (\omega_{rtot}^2 \omega_{ztot})$ .

The density of the cloud in the Mott insulator state cannot be approximated by a Thomas Fermi shape. However, by knowing the average occupancy of the lattice sites right before transition we can estimate the distribution of the number of atoms per site and use it as a guide to estimate the number of atoms in each domain after the transition. We can justify this by arguing that

for large lattice heights the tunnelling is suppressed and atoms cannot distribute themselves effectively after the Mott insulator transition. Using these simple approaches we can estimate the initial atom number to get most of the atoms in the one atom per site Mott insulator or two atom per site Mott insulator etc. To study the superfluid Mott insulator transition we would like to have most of the atoms in the one atom per site Mott insulator to be able to compare with the simplest theory. Starting with  $\approx .3$  million atoms gives us roughly 60% of the atoms in one atom per site just before the transition. For such atom numbers the path taken on the Bose Hubbard diagram is close to the path illustrated by the arrows in Fig. 3.6. It is rather hard to know the exact density and these models should be checked experimentally if possible. Photoassociation of atoms in the optical lattice is a great tool to probe site occupancy and it will be discussed in section 3.5.

We tried to adjust our lattice beam diameters such that the change in the cloud size is not big so the atoms can distribute themselves on a short time scale. The cloud still expands by  $\approx 15\%$  and the atoms need time to equilibrate. In order for the cloud to stay in equilibrium the lattice should be ramped up slowly. The tunnelling time between neighboring atoms for lattice height of  $10E_r$  is roughly 1ms so by ramping up the lattice slowly (50 ms) we can satisfy this condition of adiabaticity easily.

Tab. 3.1 shows the change in experimental parameters as we increase the lattice strength.

Lattice strength in $E_r$	$g^*/g$	$\omega_{rcom}(Hz)$	$\omega_{zcom}(Hz)$	$r_{TF}(\mu m)$	$z_{TF}(\mu m)$
0	1	20	11.6	14.2	24.5
3.9	5.464	29	17	17.16	29.59
8	9.365	36.25	22.3	17.37	29.95
10	11.07	39.3	34.3	16.6	28.62
13	13.48	43.5	27	17.35	29.91

Table 3.1: We list the increase in interaction as  $g^*/g$  as we increase the lattice strength. The combined trap frequencies as well as the Thomas-Fermi radii are listed.

### 3.3.2 Calibration of the Optical Lattice

The strength of the lattice can be calculated using our measurements of the beam waist and optical power. When we first set up the lattice we adjusted the fiber output couplers so that the radial lattice beams have the same beam waist  $\varpi_r$  and the axial lattice beam waist is  $\varpi_r/2$ . However, due to the uncertainty in our beam waist and optical power measurements the calculations need to be checked experimentally. We use two main techniques to calibrate the lattice strength. The first and easier one relies on applying the lattice beams individually for a very short period of time  $t$  ( $t \ll$  period of oscillation in the lattice site potential) [67]. This pulse splits the atomic population in different momentum components. This can be thought of as imprinting a phase variation on the atomic wave packet  $\Phi_0$ . The new wave function is  $\Phi = \Phi_0 e^{-i\alpha \cos(2kx)}$  where  $\alpha = V_0\tau/2\hbar$ , with  $\tau$  is the duration of the pulse and  $V_0$  is the strength of the optical lattice. This wave-function can be expanded into different momentum components. The ratio of the atoms in different momentum components depends on the lattice strength and pulse

duration. If we use a small enough number of atoms such that only the zeroth and first orders are populated we can estimate the lattice depth easily. The ratio of the number of atoms in the central peak to the first order peak is  $J_0^2(\alpha)/J_1^2(\alpha)$ . We can probe this ratio with TOF images and calibrate the lattice potential for each direction. This calibration was within 20% of the calculated value. The main uncertainty in our measurement comes from the uncertainty in the power measurement. The power of the short pulse is measured using a photodiode that picks up a tiny reflection of the lattice beam from a window. The signal is digitally read by an oscilloscope but there is an over-shoot that may yield a 10% error in the scope's reading. The second method that relies on photoassociation is harder and will be covered in section 3.5. Note that we had a photoassociation setup ready for another experiment, otherwise using photoassociation for lattice calibration is too laborious.

### 3.4 Probing the Phase Transition with Bragg Spectroscopy

As mentioned earlier ultra-cold atoms in optical lattices allow us to study solid-state-like systems with accurate experimental control of parameters, one example being the superfluid-Mott insulator transition [28]. Even though the interactions between atoms can be changed smoothly by changing the intensity of optical lattice lasers, the opening of the excitation gap has eluded experimental verification [28, 29]. The interference experiments that probe the phase coherence of atoms show a gradual transition. The tilting of the lattice by Greiner *et al.* [28] and the shaking of the lattice by Stoferle *et*

*al.* [29] to observe the Mott gap could not detect the vanishing of the gap near the phase transition. According to mean field theory the gap scales as  $(U - U_c)^{1/2}$  [26] near the transition. Oosten *et al.* has proposed to use Bragg spectroscopy to measure the particle hole excitations in the Mott insulator [30]. They calculate the scattering rate from the Bragg beams and show results for the response of the system. Their results show that the gap grows linearly with the on site interaction energy  $U$  when deep in the Mott insulator state, and closes as

$$E_g \propto \sqrt{U - U_c + \eta q^4} \quad (3.15)$$

for  $U$  close to  $U_c$ , where  $U_c$  is the on site interaction energy at the transition point,  $q$  is the momentum transfer from the Bragg beams, and  $\eta$  is a positive function of  $U_c$  and  $J$ , the hopping term in the Bose-Hubbard model. Note that in the case of zero momentum transfer this result is the same as the mean field calculation for the opening of the excitation gap ( $\sqrt{U - U_c}$ ). Another theoretical paper also studied the Bragg spectroscopy of the Mott insulator and emphasizes this method's ability to measure the particle hole excitations [52].

### 3.4.1 Bragg Spectroscopy of the Mott Insulator

We followed the suggestions of Stoof *et al.* to measure the excitations of the Mott insulator by Bragg spectroscopy. The Bragg beam setup is as described in section 2.2. We load the BEC into the optical lattice, ramp up the lattice over 50 ms to  $V_0$ , and apply the Bragg beams for a duration  $\tau$ .

Then we ramp down in 20ms to zero lattice height and wait for 5 ms for the cloud to thermally equilibrate. Then we turn off the magnetic trap, allow the cloud to expand for 24 ms, and take an image. We fit this cloud to the model described in section 2.4.2 to determine the temperature of the system. The Bragg beams' frequency difference  $\omega$  is changed and the experiment repeated to see the temperature increase of the system for different  $\omega$ . The excitations created by the Bragg pulse are damped into the system as heat and shows up as an increase in the temperature. After completing a scan for a certain  $V_0$  we repeat the same experiment for different values of  $V_0$ . The Bragg beams each had an intensity of  $\approx 180$  mW/cm<sup>2</sup> and a detuning of  $\approx 430$  GHz from the <sup>87</sup>Rb D-1 line. The results of the scan are plotted in figs. 3.7-3.9.

What we observe in the plots is very instructive in understanding the nature of the transition. If there is energy transferred to the system due to particle-hole resonance the temperature increases and the BEC fraction decreases. When we do the same experiment without the Bragg pulse we can recover a BEC fraction of  $\approx 70\%$ . In the superfluid region there is no gap in the particle-hole excitation spectrum and we expect to see a decrease in BEC fraction (excitations) for a broad range of  $\omega$ . In the Mott insulator region however, the particle-hole excitation spectrum has a gap and there should be no excitations for energy transfer up to the gap ( $\hbar\omega < E_g$ ). For  $V_0 = 11.5E_r$  (Fig. 3.7) we see that there is a dip around  $\omega/2\pi = 1\text{KHz}$ , for  $\omega/2\pi < 1\text{KHz}$  there are some excitations and for  $\omega/2\pi > 1\text{KHz}$  the excitations are suppressed. We think this is due to the co-existence of the



superfluid and Mott insulator domains. The superfluid is excited for low  $\omega$  and the Mott insulator is excited at  $\omega/2\pi = 1\text{KHz}$ . For higher  $\omega$  there is no transfer of energy and the BEC fraction increases. The superfluid excitation resonance gets smaller with increasing lattice height. Thus, high frequencies ( $\nu_i 3\text{ kHz}$ ) are far from the superfluid excitation resonance and the superfluid is not excited as can be seen in figs. 3.7-3.9. To show that the dip in the Bragg spectra is due to the Mott insulator we plot the scan before and after the transition on the same graph in Fig. 3.11. From this plot it is clear that the dip occurs only for stronger lattice (Mott insulator regime). As we go to higher lattice heights we see that there is a peak due to the Mott insulator and the excitations get smaller and smaller for lower  $\omega$  (Fig. 3.8, Fig. 3.9). To understand this we can go back to the Bose-Hubbard phase diagram in Fig. 3.6. The center of the cloud has a density represented by the dark horizontal arrow in Fig. 3.6. As the lattice height is increased close to the transition point into the one atom per site Mott insulator, the center of the cloud is superfluid as is the edge of the cloud and a very small portion in between is in a Mott insulator state. Thus, there are a lot of excitations still due to the superfluid. As we increase the lattice strength further into the Mott insulator domain the superfluid fraction decreases and the excitations due to the superfluid are suppressed. For the Mott insulator region the excitation gap corresponds to a transfer of energy equal in the vertical direction in  $\mu_i = \mu - \epsilon_i$  which is  $U$  for  $U \gg J$  as explained earlier (see Fig. 3.5). In our Bragg spectra this would correspond to the left edge of each peak. To acquire the edge from our data,

we exclude the sharp peak corresponding to the Mott insulator and fit the rest with a polynomial. Then we fit the sharp left edge of the peak with a straight line and take the intersection of two fits to be the particle-hole gap (Fig. 3.12). We can see from the phase diagram that this gap goes to zero as we approach the superfluid region from the Mott insulator region. We plot the particle hole gap as a function of lattice height and note that the gap decreases more sharply close to the transition (Fig. 3.10). We try to fit the opening of the gap to mean field calculation by Oosten et al. [30] that predicts the gap does not go to zero at the transition (eq. 3.16). We plot our data where we convert the lattice strength  $V_0$  in Fig. 3.12 to  $U$  and fit according to eq. 3.16. (Fig. 3.13. The fit gives a transition lattice strength of  $V_0 = 11E_r$ . Mean-field calculations predict a transition at  $V_0 = 12.5E_r$ . This falls within our measurement uncertainty of  $\approx 15\%$  in  $V_0$  in  $V_0$ . This is the first observation of the nonlinear opening of the Mott gap. The particle-hole gap can be measured very accurately as can be seen from the plots. Our experiments establish Bragg spectroscopy as a powerful tool in probing quantum phase transitions. Accurate measurement of the particle-hole gap also has a future application for quantum information processing as the fidelity of a Mott state is given by this gap [30].

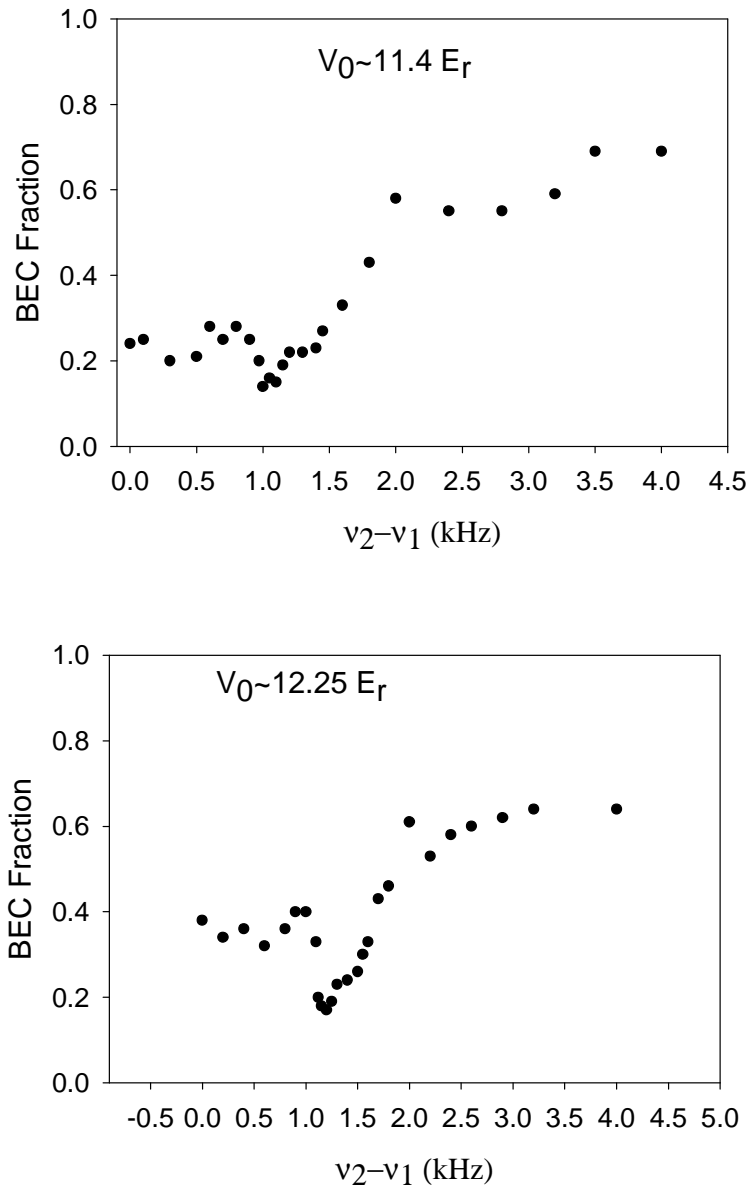


Figure 3.7: BEC fraction of a Bragg-excited gas as function of excitation energy. These data are taken in a regime in which the gas contains both superfluid and insulating components. The excitations for low  $\omega$  are due the superfluid. The dip is attributed to the Mott insulator.

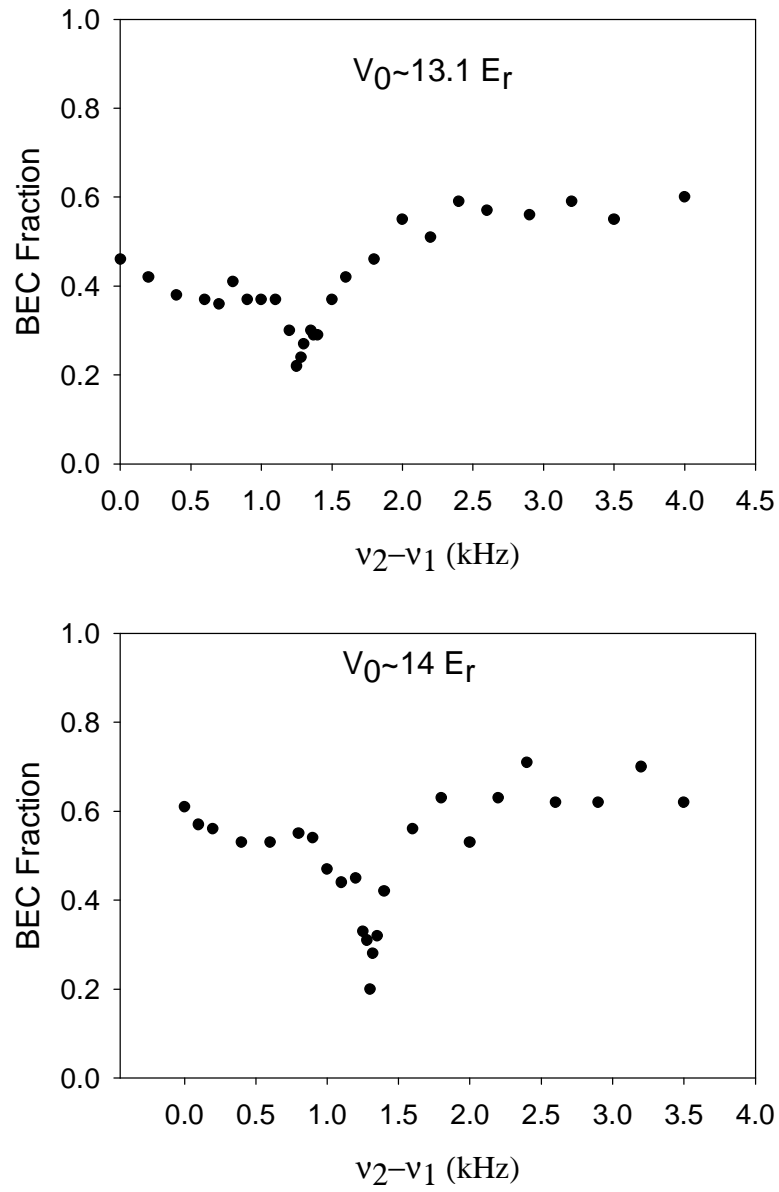


Figure 3.8: BEC fraction of a Bragg-excited gas as function of excitation energy. The superfluid fraction and the excitations due to the superfluid are decreasing as we increase the lattice strength. The peak due to the Mott insulator is more evident.

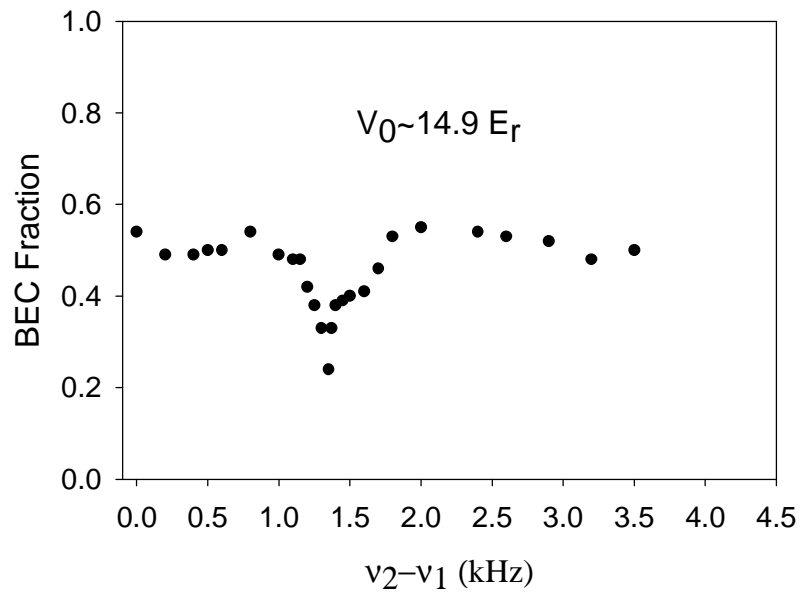


Figure 3.9: BEC fraction of a Bragg-excited gas as function of excitation energy. The superfluid fraction is negligible at this lattice strength as we cannot see any excitations other than the Mott insulator.

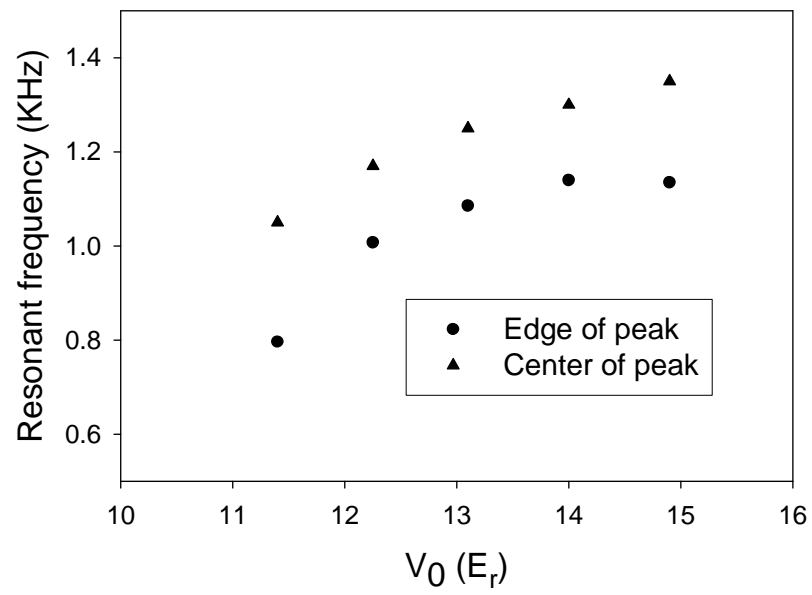


Figure 3.10: Bragg resonance falls sharper as we get close to the superfluid region. This is due to the parabolic shape of the tip of the Mott lobes.

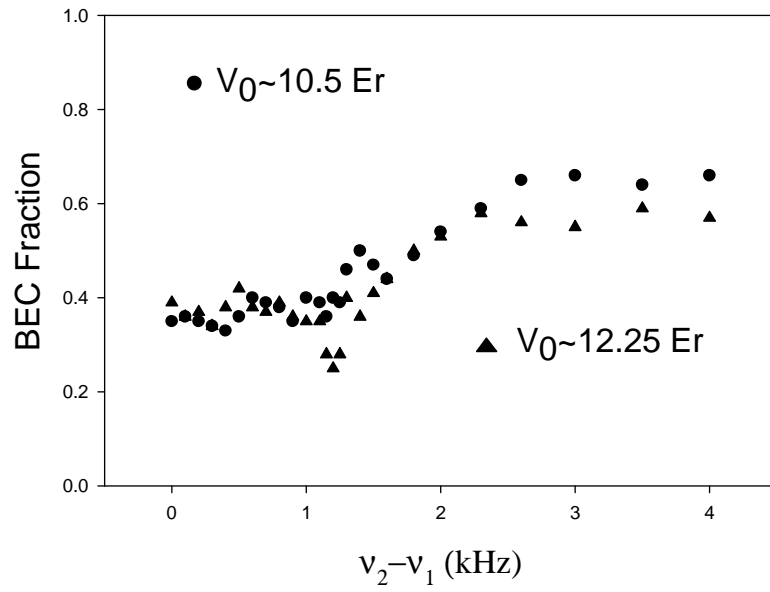


Figure 3.11: Before the transition ( $V_0 = 10.5E_r$ ) the superfluid has no dip. After the transition ( $V_0 = 12.25E_r$ ) the dip is contributed to the Mott insulator.

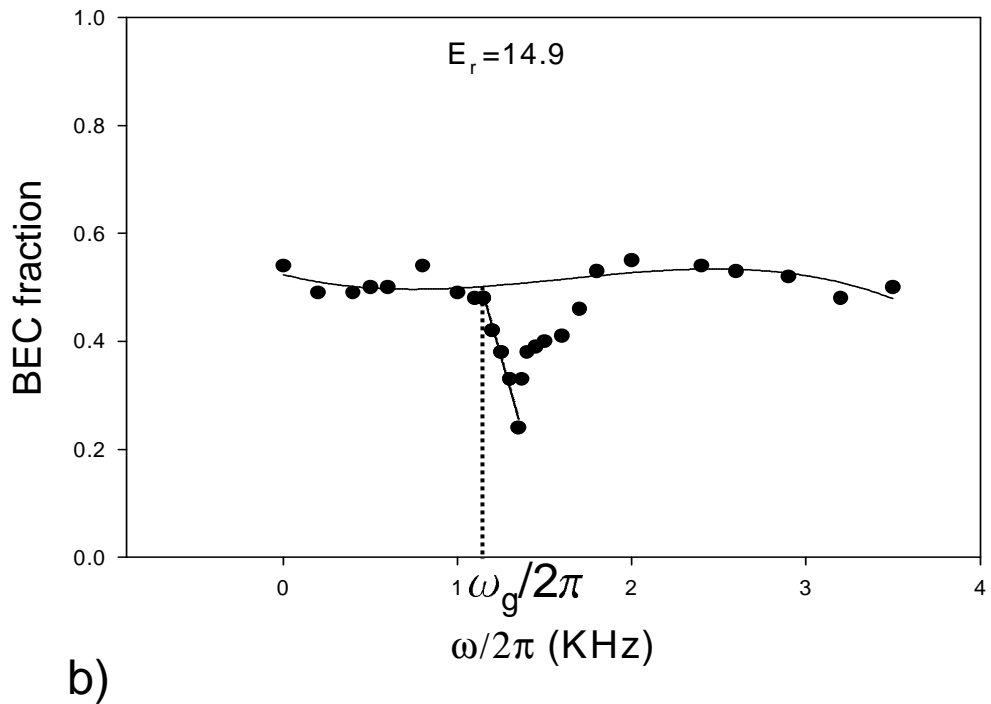
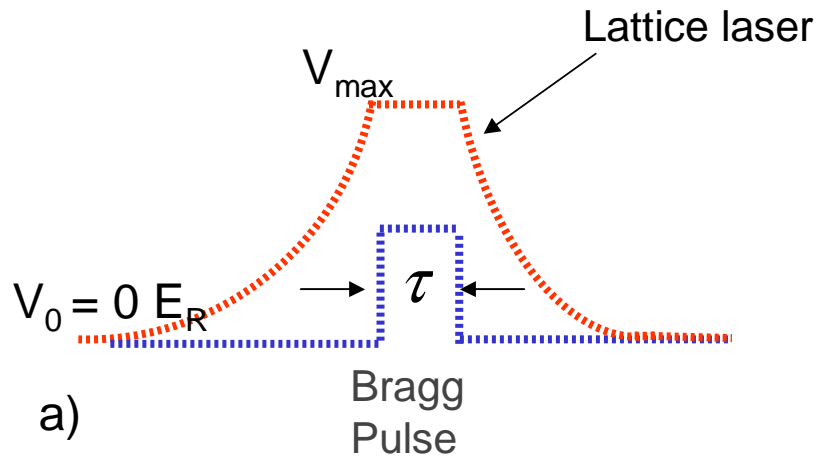


Figure 3.12: a) Lattice and Bragg laser beam intensities as a function of time. The duration of Bragg pulse is 10ms. b) Fitting of the scan. After the peak is excluded the rest is fit to a polynomial. Then the left sharp edge of the peak is fit with a straight line and the intersection of the two fits (dashed line) is taken as the particle-hole gap given by  $E_g = \hbar\omega_g$ .



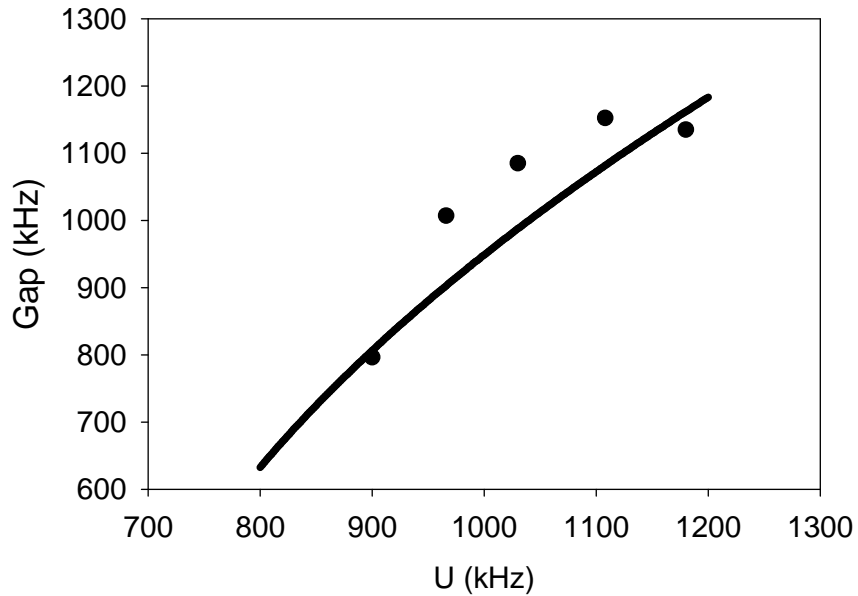


Figure 3.13: The circles are the same data points as in Fig. ?? converted to  $U$ . The line is fit to the data points with a function of the form  $\Delta = \alpha\sqrt{U - U_c + \Delta_0}$ .  $\Delta_0$  was chosen to be a constant. The fit gives a transition value  $U_c = 870$  Hz which corresponds to  $V_0 = 11E_r$ . The transition is expected to occur at  $V_0 = 12.5E_r$  according to mean field calculations. This is within our measurement uncertainty of  $\approx 15\%$  in  $V_0$ . At the transition the gap is  $\Delta_0 \approx 700$  Hz.

## 3.5 Photoassociation Experiments in the Mott Insulator

After the successful observation of atomic BEC researchers set a new goal of realizing molecular BEC [51, 68, 69]. Jaksch et al. proposed photoassociation (PA) of a Mott insulator of bosonic atoms in optical lattices to create molecular BEC [70]. PA involves the coupling of two atoms to an excited molecular level via an absorption of a photon [71]. A Mott insulator in optical lattice provides an ideal framework for PA experiments due the constant high densities in the Mott domains. In this section we report new data taken for PA experiments reported in Changhyun Ryu's thesis [51] and show how PA can be used to probe the distributions of Mott insulator domains and calibrate the lattice strength.

### 3.5.1 Single Photon Photoassociation of Mott Insulator

When the atoms are in a deep optical lattice, atoms in different lattice sites are spatially separated and cannot be coupled by PA easily. If there is more than one atom in a lattice site the atoms can readily PA to form a molecule. These molecules are detectable as missing atoms and we can measure the number of atoms with a TOF image. Thus, if we shine a PA laser resonant with a bound excited molecular level we expect that the multiply occupied sites decay very fast until we are left with single or no atoms in each lattice site. We used this method to obtain decay curves of the atom number vs PA pulse duration in a deep optical lattice ( $V_0 = 20E_r$ ). For atom numbers

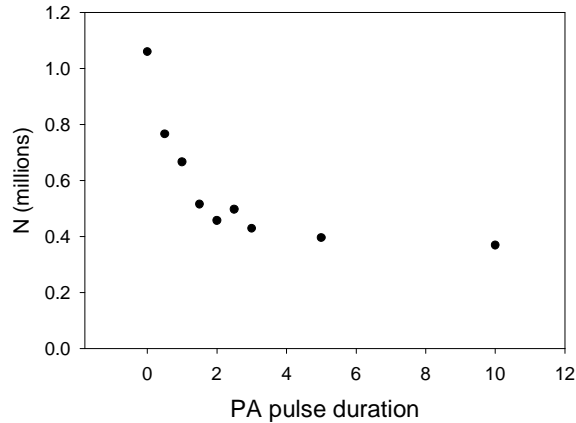


Figure 3.14: Number of remaining atoms in a Mott insulator as a function of the duration of a photoassociation pulse. Multiply occupied sites readily photoassociate yielding trap loss. The atom number decreases from 1 million to .4 million over 2 ms due to multiply occupied sites. After 2ms the atoms number decays very slowly due the fact that unit occupancy sites are decoupled from each other and do not photoassociate.

$N > .15$  million there is a very fast decay (Fig. 3.14) followed by a very slow decay. The fast decay must be coming from multiply occupied sites, and the slow decay probably due to the single occupied sites in the system. Using this method we can at least determine down to which atom number there is still a two atom per site Mott insulator domain. Our results indicate that down to .15 million atom numbers there are doubly occupied lattice sites.

### 3.5.2 Raman Photoassociation of a Mott Insulator

Extensive work has been done on producing ultra-cold molecules [72–75]. Our group has concentrated on efforts to produce ultra cold molecules by photo-association [69] in the BEC. However, these molecules are very short lived due to inelastic collisions between atoms and molecules. One way around

this problem is to use ultracold atoms in optical lattices. If each lattice site is occupied by two atoms, then they can be converted to one molecule in each site via two color photoassociation (PA). Jaksch et. al. suggested to use two atom per site Mott domains in optical lattices to create molecules by PA and then melt the lattice to make a molecular BEC [70]. These molecules do not suffer from collisional losses and provide an ideal method for ultra-cold molecule formation. Raman photo-association of  $^{87}\text{Rb}_2$  molecules in a Mott insulator state was carried out in our group and is described in detail in [51]. Here I give a brief review of the experiment and report the new data we obtained for the same experiment.

Raman PA of a BEC was carried out to produce ultra-cold molecules in a certain ro-vibrational molecular state [69]. A schematic of the process is shown in Fig. 3.15. Two atoms can be coupled to a molecular ground state level by absorbing a photon from the first laser ( $\omega_1$ ) and emitting a second photon into the second beam ( $\omega_2$ ) by stimulated emission. The frequency of the first beam is detuned ( $\delta_1$ ) from the intermediate excited molecular level to minimize off resonant scattering. The detuning of the second laser ( $\delta_2$ ) is such that  $\omega_2 - \omega_1 = \epsilon$ , the binding energy of the target ro-vibrational molecular state [69]. The disadvantage of this method is the inelastic collisions between atoms and molecules. Atoms in a Mott insulator are localized to individual lattice sites and molecules produced in a lattice site will not suffer from collisions with atoms in other lattice sites. We need two atoms per site to make a molecule, therefore two atoms per site Mott insulator will be the ideal tool for

efficient production of molecules. As mentioned earlier because the system is inhomogeneous the complete system cannot be in two atoms per site Mott insulator. We can try to maximize the number of atoms in the two atom per site Mott insulator. A calculation similar to the one described in sec. 3.3.2 can be done to estimate the ideal atom number. An important peculiarity of the Mott insulator is the difference in interaction energy between two atoms per site and three atoms per site. Two atoms per site has an on site interaction energy of  $U_{a-a}$  while three atoms per site has an on site interaction energy of  $3U_{a-a}$ . If we photoassociate two atoms in a lattice site and make a molecule there is no on-site interaction energy. On the other hand photoassociation of three atoms in a lattice site results in a molecule and an atom in that site with an on-site interaction energy  $U_{a-m}$  between the atom and the molecule. This results in a difference in the resonant frequencies of two atom sites and 3 atom sites given by

$$\hbar\omega_{3Raman} - \hbar\omega_{2Raman} = 2U_{a-a} - U_{a-m}. \quad (3.16)$$

We load the BEC in a deep lattice ( $V_0 \approx 18E_r$ ) where it is deep in the insulator phase and do Raman scan to observe the creation of molecules. The experiment is described in detail in [51]. We are driving transitions to the  $v = 39$  vibrational state in the triplet ground state. This state has a binding energy of 636.0094 MHz. The detuning from the intermediate level is 3.9 GHz. Our PA beams have a total power of  $\approx 70$  mW.

The result of the scan is shown in Fig. 3.16a. We observe the frequency

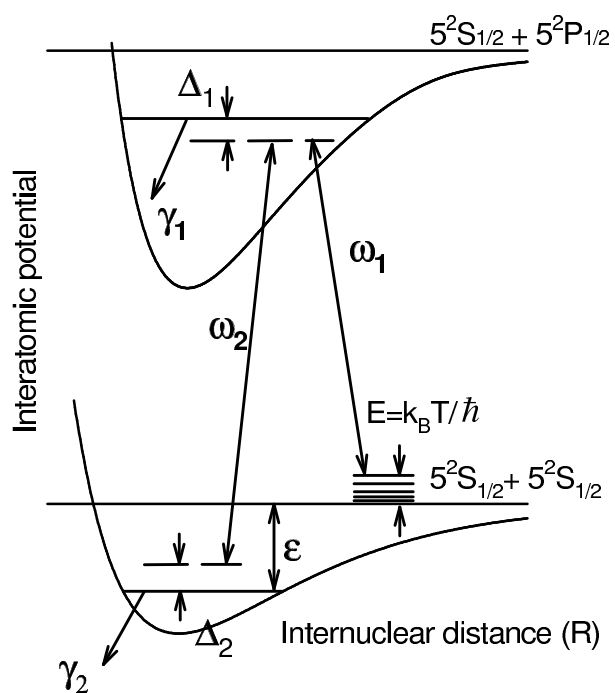


Figure 3.15: Two color Raman photoassociation schematic. This process is described in detail in [68].

difference between the two atom per site Mott insulator and the three atom per site Mott insulator. These scans can be used to determine  $U_{a-m}$  and the atom-molecule scattering length. Work is under way for accurate calculation of these values using Wannier functions to calculate the ground state energy of the system. Note also that by fitting our scan we can determine the percentage of the atoms in each domain. This is a very powerful tool in determining the distribution of the atoms. We used the results of these scans to tune our initial atom number to adjust relative populations of different Mott domains. As mentioned earlier the most efficient molecule formation will be with a maximal two atom per site Mott state. We can get about 40% of atoms in the two atoms per site domain as seen in Fig. 3.16b. Coupling two atoms in a deep lattice site to molecules via Raman photoassociation can be a coherent process. All the atoms in the two atom per site Mott insulator will be converted to molecules with a  $\pi$  pulse, and back to atoms with another  $\pi$  pulse exhibiting Rabi oscillations between atoms and molecules. We observed this experimentally as reported in [51] by locking the Raman frequency to the two atom per site resonance and varying the duration of the pulse. The data along with a fit is shown in Fig. 3.17. We can observe up to 4 oscillations between atoms and molecules, the dips in atom number corresponding to molecules and peaks to the atoms. Raman-induced Rabi oscillations provides a possible route to studies of degenerate molecular gases. In our setup this would involve melting the lattice after forming molecules to create a degenerate molecular gas. The molecules need to be in ground ro-vibrational state which may be

achieved with an additional Raman scheme.

There is a zero point energy in a lattice site due to the tight confinement. This zero point energy increases with increasing lattice height causing a shift of the Raman resonance frequency. This shift in Raman frequency can be used to calibrate the strength of the lattice beams. The zero point energy shift due to the lattice is

$$\Delta E = \frac{3}{2}\hbar\omega_0 \quad (3.17)$$

where  $\omega_0$  is the harmonic trapping frequency of the lattice site given by  $V_0 \sin^2(kx) = 1/2m\omega_0^2 x^2$ . This number is 29.8 kHz for  $V_0 = 20E_r$ . We apply the three lattice beams one by one, and perform Raman spectroscopy to find the resonant frequency. Thus, we can calibrate the strength in each direction by looking at the Raman resonance frequency shift to obtain equal strengths in each direction.



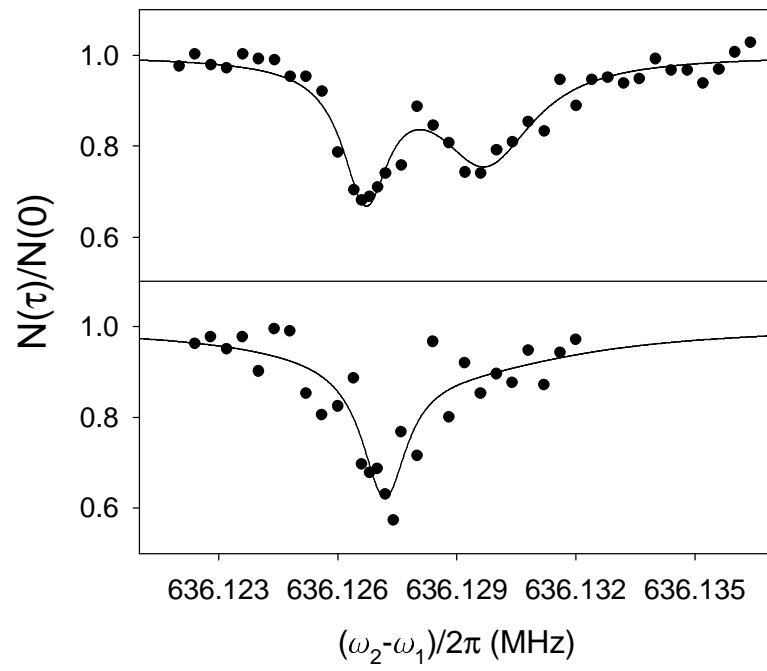


Figure 3.16: a) Raman scan with .5 million atoms showing frequency shift between  $N=2$  and  $N=3$  Mott insulators. b) Raman scan with .25 million atoms

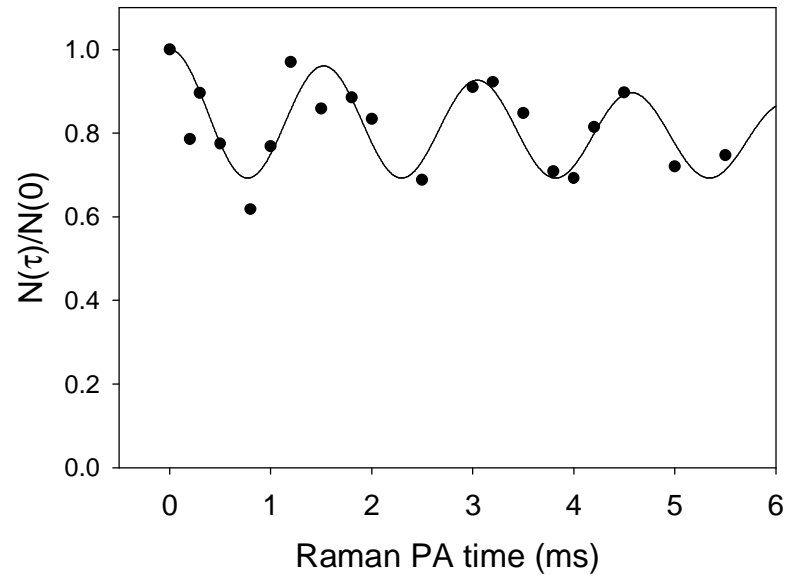


Figure 3.17: Rabi oscillations between atoms and molecules. The number of atoms is .3 million, the total PA power is 75 mW (the first PA beam power is 55 mW and the second PA beam power is 20 mW), the detuning is -3.9 GHz, and the optical lattice depth is  $18E_r$ .

## Chapter 4

### Conclusion

This thesis presents results of experimental studies of excitations of quantum gases in optical lattices. By loading a BEC of  $^{87}\text{Rb}$  into an optical lattice the interactions between the atoms were changed by changing the lattice strength. A quantum phase transition from a superfluid to a Mott insulator was realized. Both the superfluid and the Mott insulating state excitation spectra were measured using Bragg spectroscopy.

This gives us valuable data as we try to understand the nature of strongly interacting superfluid.

Ultracold atoms in optical lattices is a simple but perfect realization of the Bose-Hubbard model, that predicts a quantum phase transition at a critical lattice strength. Bragg spectroscopy allows the transfer of a controlled amount of energy into the system which enables particle-hole excitations. Mott insulator exhibits a gap in its excitation spectrum which was measured very accurately using Bragg spectroscopy. This allowed us to observe the opening of the gap close to the transition. Our results establish Bragg spectroscopy as a powerful tool to study quantum phase transitions.

The measurement of the particle-hole gap is also important for the

application of Mott insulator state for quantum information systems. The fidelity of the Mott state is determined by the particle-hole gap [30]. Thus, Bragg spectroscopy is already a proven candidate for measuring the fidelity of such systems.

We have observed Rabi oscillations between atoms and molecules. This is a first step toward realizing a molecular condensate with bosonic atoms. This would involve melting the lattice which requires molecules to be in ro-vibrational ground states. To transfer molecules from high vibrational states to ground ro-vibrational state may be possible with an additional Raman scheme. The complexity of the experiment will be the limiting factor in realizing stable conditions.

## Appendix

# Appendix 1

## Lithium Setup

In this chapter I describe the progress toward a rubidium-lithium experiment. The laser system for lithium and the addition of lithium to the rubidium apparatus is described.

### 1.1 Two Species

Study of degenerate two species systems has a variety of interesting applications. For example hetero-nuclear polar systems has long been suggested for permanent electric dipole moment (EDM) investigation [76]. To increase the sensitivity of the system it is important to have the molecules in a particular state. A good way of producing molecules in a specific state is photo-association [71]. Thus production of ultra-cold molecules from two species will provide an ideal system for EDM search. Another interesting phenomena is the transition of fermionic atoms to a superfluid state of Cooper pairs [77]. The reason we need two species systems to study degenerate fermions is because evaporative cooling needed to cool alkalis to quantum degeneracy does not work well for fermions. The reason is evaporative cooling relies on binary collisions and at ultra-low temperatures this process is governed by quantum

statistics. Fermions have anti-symmetric two particle wave functions, so s-wave collisions are forbidden while higher order collisions are suppressed at low temperatures. So far achieving quantum degeneracy in fermions relied on sympathetic cooling [78–82]. This involves the thermalization of fermions by a another colder species. The other distinguishable species can be different isotopes of the same element, two different spin states of the same isotope or even two different chemical elements. There is already some theoretical work that shows the BCS phase transition of fermions in an optical lattice can be reached experimentally [83]. Fermionic lithium cooled by rubidium can be an ideal system to study this phase transition. Cooling  ${}^6\text{Li}$  with rubidium has advantages over cooling it with another state of  ${}^6\text{Li}$  or the bosonic  ${}^7\text{Li}$ . The disadvantage of using two fermionic states for evaporative cooling is the reduced cooling rate at lower temperatures and the fact that both species are evaporatively cooled leading to much smaller fermionic samples. The advantage of rubidium over  ${}^7\text{Li}$  is the big mass difference. Because rubidium mass is so much heavier than lithium the latter enters quantum degeneracy at higher temperatures. Thus, if we thermalize lithium with a BEC of  ${}^{87}\text{Rb}$  we can easily reach deep quantum degeneracy for lithium ( $.1T_F$ ).

## 1.2 Lithium Laser System

The laser system is based on a master-slave injection locking setup Fig. 1.1. The master laser is a homemade Littrow laser that employs a 30mw Phillips (model:CQL806/30) laser diode and a 954 aluminum bronze housing.

The stability of the system is remarkable. After the initial tuning the laser stayed on resonance over five years without the need to tune any knobs. The laser is temperature controlled using a TE cooler. We only get about 15mW of power from the laser as  $\approx 30\%$  is reflected back into the diode from a holographic grating. The slave lasers are employed to get more power. The frequency of the master laser is locked to the cross-over resonance from the Lamb-dip setup. The output is split into two and the frequency is shifted up and down by half the ground state hyperfine splitting to injection lock the repumper and the MOT slave lasers respectively. The frequency shift is accomplished by double-passing each beam through an AOM. The master laser and the two slaves were originally used to trap  ${}^7\text{Li}$  ([84]). To modify the system for  ${}^6\text{Li}$  we simply replaced the AOMs that had a center frequency of 200 MHz with new AOMs with a center frequency of 115MHz to compensate for the difference in the hyperfine splitting. We also decided to use more power for the slower laser to saturate the transition. Therefore, we added two more slave lasers to the setup. The first one is injection locked to the MOT laser. The output of this laser is fed into a four pass through a 350MHz AOM to shift its frequency by 1.4878GHz to the red to compensate for the Doppler shift of the atoms coming out of the source. After the four pass we only have 5mW of power so we injection lock the other slave to get 25mW of power for the slower laser beam.



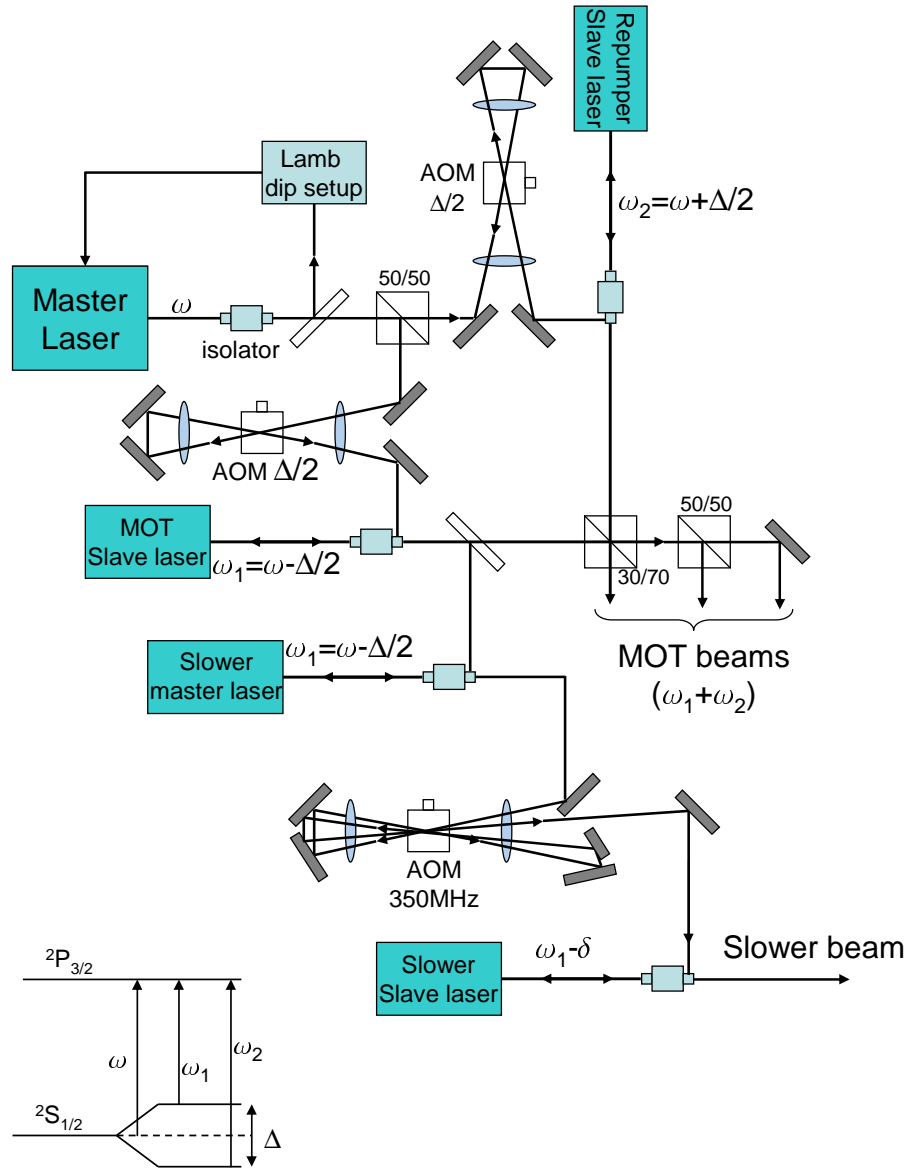


Figure 1.1: Lithium laser setup is based on a master-slave laser scheme. The master laser is locked to the cross-over signal from the lamb dip setup. The master laser beam is split into two and shifted up and down by half the hyperfine splitting  $\Delta$  to lock the MOT and repumper slave lasers respectively. Another slave is locked to the MOT slave laser and its output is frequency shifted by  $\delta$  in a four pass setup and injection locked into another slave which provides the slower laser.

### 1.3 Two Species Zeeman Slower

We considered several options in realizing the the two species trap. The ultimate cooling into quantum degeneracy would have to be in the already running rubidium chamber. One of the options was to use the lithium Zeeman slower and chamber that demonstrated efficient lithium MOT loading to get a lithium MOT [84]. Then we would transfer lithium into the rubidium chamber using a low-velocity intense source LVIS setup first demonstrated by Lu et al. [85]. The other option was to use the lithium Zeeman slower to directly load a lithium atomic beam into the rubidium chamber. Both of these methods would have cut down the available optical access of the system and required considerable vacuum work. Therefore, we went with a third option that involved making a two species atomic beam and slowing them with the rubidium Zeeman slower.

This ideas was inspired by the work of Hadzibabic et al. [86] where they loaded a two species MOT from a two species atomic beam slowed in the same Zeeman slower. Our two species oven design is similar to this groups as sketched in section 2.7. The main difference is our setup is that we want to add lithium into a rubidium system as opposed to a sodium system. This creates extra difficulty in using the same slower due to the big mass difference. The maximum deceleration is given by

$$a_{max} = v_{rec} \times \frac{\Gamma}{2}. \quad (1.1)$$

Even though the maximum scattering rate  $\Gamma/2$  is comparable for lithium and

rubidium the big mass difference gives a much bigger recoil velocity  $v_{rec}$  for lithium compared to rubidium resulting in a ratio of

$$\frac{a_{max}^{Li}}{a_{max}^{Rb}} = \frac{18 \times 10^5 m/s^2}{10^5 m/s^2} \quad (1.2)$$

in maximum deceleration. A value of  $0.6a_{max}$  is chosen to provide stable slowing conditions. Thus, a slower designed to operate at  $0.6a_{max}^{Rb}$  rubidium will be very inefficient for lithium slowing and vice versa. The Zeeman slower is designed to cancel the Doppler shift throughout the slowing region such that the atoms are always resonant with the slower laser [87]. A  $\sigma^-$  slower (increasing field requires the velocity along the z axis to satisfy [88]

$$v(z) = \lambda \left( -\frac{\mu_b}{h} B(z) - \delta \right). \quad (1.3)$$

For constant deceleration  $a$ , this gives a magnetic field profile along the z axis

$$B(z) = -B_o - B_1 \sqrt{1 - 2az/v_i^2} \quad (1.4)$$

where  $B_o = h\delta/\mu_B$ ,  $B_1 = hv_i/\lambda\mu_B$ , and  $v_i$  is the initial velocity of the atoms that will be captured. The rubidium Zeeman slower was based on this design with  $a = 0.6a_{max}$ , the detail of which are given in [43]. In order to slow both species we have to pulse loading where we alternate the current in the coils of the slower to produce a different field profile for each species. This allows us to get a deceleration of  $a = 0.6a_{max}$  for each species. The slower was designed for rubidium and thus had 18 gauge coils for the tapered coils [43] which are not desirable for lithium as this species requires steeper magnetic field profile meaning higher currents through the tapered coils. These factors were taken

into account in determining what current to use in the bias and tapered coils in order to get efficient slowing ( $a = 0.6a_{max}$ ) for lithium and not burn out the coils. The field generated by the coils is calculated using a Matlab program. The result is plotted in Fig. 1.2 along with the magnetic field profile given by eq. 1.4.

## 1.4 Loading the Two-Species Source into the Chamber

One of the main reason in choosing a dual species atom source and common slower design was the minimum amount of vacuum required. The source part of the chamber is separated from the UHV part by a gate valve allowing venting of the source side without disturbing the UHV part. The idea is to vent the source side to argon replace the rubidium atom source with the dual species atom source and pump down without a bake-out.

Lithium is not commercially available in glass vacuum ready ampules as rubidium. Therefore, certain steps need to be taken to prepare lithium for vacuum environment. Lithium sample is preserved and shipped in mineral oil to prevent it from reacting with air. Mineral oil is detrimental to vacuum and must be cleaned from the system. This is done by rinsing lithium in petroleum ether in an argon filled glove-bag. Small amount of oxidization is present on the lithium surface in mineral oil and this is removed with a metallic brush. To clean the lithium further we need to do a preliminary bake-out. The clean lithium is placed in the dual-species oven structure without the rubidium and vacuum sealed inside the argon filled glove-bag. Then, it is rushed to pumping

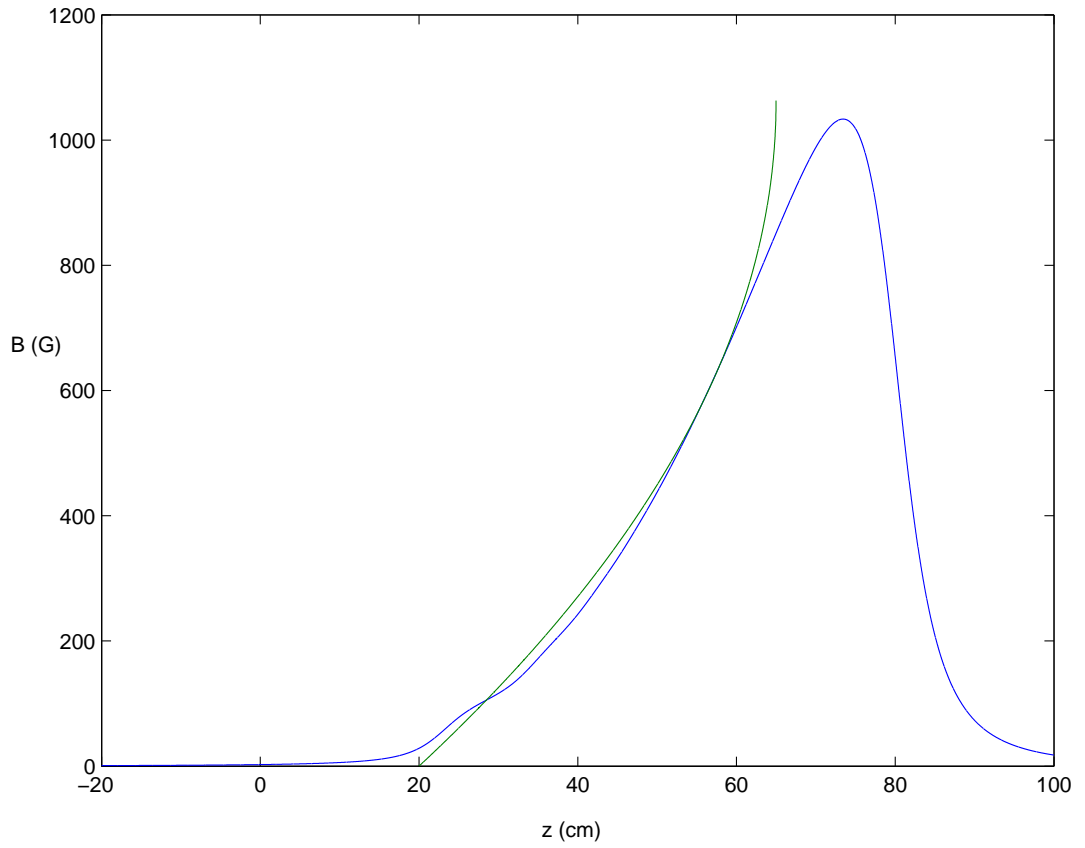


Figure 1.2: The blue curve is the calculated field profile generated by the coils. The green curve is given by eq. 1.4. The tapered coil current is  $I_{tapered}=8.5\text{A}$  and the bias coil current is zero to limit power dissipation to  $P=1.25\text{KW}$ . The detuning  $\delta=1.4878\text{GHz}$  and  $v_i=998\text{m/s}$ .

station consisting of a mechanical and diffusion pump. The atom source is sealed except for the 2mm hole in the nozzle. Because the source is filled with argon, the diffusion of air through the tiny nozzle is negligible and oxidization shouldn't occur during the transfer to the pump station. The lithium is baked up to 500°C for two days. We always keep the nozzle temperature at least 30°C higher than the lithium temperature to avoid clogging. After the bake-out, the oven is cooled slowly and the system is vented to argon. The oven is rushed to an argon filled glove-bag where the section containing rubidium ampule is attached and is kept there until the UHV system is ready. The UHV chamber is sealed with the gate valve. The source side is vented to argon, the existing oven is removed and immediately replaced with the new oven containing lithium. The UHV system is pumped down using a pump station and the new source is ready to be used. We first replaced the rubidium oven with a dual species oven containing rubidium and  $^7\text{Li}$ . We had in mind hetero-nuclear photo-association experiments. Later we decided to use fermionic  $^6\text{Li}$  instead and ordered  $^6\text{Li}$  from Icon Isotopes. Unfortunately, the shipment contained pure  $^7\text{Li}$  instead which was determined by absorption experiments in a Lamb dip setup. Thus, we ended up replacing the  $^7\text{Li}$  with  $^7\text{Li}$  that cost us a lot of time. This was a major set back and the lithium experiment didn't materialize as we decided to push ahead with rubidium experiments in the mean time.

## Bibliography

- [1] P. Kapitza, *Nature* **141**, 74 (1938).
- [2] J.F. Allen and J.D. Misener, *Nature* **141**, 75 (1938).
- [3] F. London, *Nature* (London) **141**, 643 (1938).
- [4] A. Einstein, Sitzungsbericht der Preussischein Akademie der Wissenschaften, p. 3,(1925).
- [5] S. N. Bose Z. Phys 26, 178(1924).
- [6] N. Bogolubov, J. Physics(Moscow) **11**, 23 (1947).
- [7] E. C. Svensson and V. F. Sears, Progress of low temperature physics, Vol XI, ed. D.F. Brewer, (North Holland,Amsterdam,187).
- [8] M. H. Anderson, J. R. Ensher, M. R. Matthews, C. E. Wieman and E. A. Cornell, *Science* **269**, 198 (1995).
- [9] K. B. Davis, M. O. Mewes, M. R. Andrews, N. J. van Druten, D. S. Durfee, D. M. Kurn and W. Ketterle, Phys. Rev. Lett. **75**, 3969 (1995).
- [10] D. S. Jin, J. R. Ensher, M. R. Matthews, C. E. Wieman, and E. A. Cornell, Phys. Rev. Lett. **77**, 420 (1996).

- [11] M. O. Mewes, M. R. Andrews, N. J. van Druten, D. M. Kurn, D. S. Durfee, C. G. Townsend, and W. Ketterle, *Phys. Rev. Lett.* **77**, 988, (1996).
- [12] M.R. Andrews, D.M. kurn, H.J. Miesner, D.S. Durfee, C.G. Townsend, S. Inouye, and W. Ketterle, *Phys. Rev. Lett.* **79**, 553 (1997).
- [13] M. R. Matthews, B. P. Anderson, P. C. Haljan, D. S. Hall, C. E. Wieman, and E. A. Cornell, *Phys. Rev. Lett.* **83**, 2498 (1999).
- [14] K. W. Madison, F. Chevy, W. Wohlleben, and J. Dalibard, *Phys. Rev. Lett.* **84**, 806 (2000).
- [15] F. S. Cataliotti, S. Burger, C. Fort, P. Maddaloni, F. Minardi, A. Trombettoni, A. Smerzi, M. Inguscio, *Science* **293**, 843 (2001).
- [16] E. P. Gross, *Nuovo Ciminto*, 20, 454 (1961); L. P. Pitaevskii, *Sov. Phys. JETP* 13, 451 (1961).
- [17] J. M. Vogels, C. C. Tsai, R. S. Freeland, S. J. J. M. F. Kokkelmans, B. J. Verhaar, and D. J. Heinzen, *Phys. Rev. A* **56**, R1067 (1997).
- [18] S. L. Cornish, N. R. Claussen, J. L. Roberts, E. A. Cornell, and C. E. Wieman, *Phys. Rev. Lett.* **85**, 1795 (2000).
- [19] Elizabeth A. Donley, Neil R. Claussen, Sarah T. Thompson Carl E. Wieman *Nature* **417**, 529 (2002).



- [20] P. Verkerk, B. Lounis, C. Salomon, C. Cohen-Tannoudji, J. Y. Courtois, and G. Grynberg Phys. Rev. Lett. **68**, 3861 (1992).
- [21] O. S. Jessen, C. Gerz, P. D. Lett, W. D. Phillips, S. L. Rolston, R. J. C. Spreeuw, and C. I. Westbrook, Phys. Rev. Lett. **69** 49 (1992).
- [22] A. Hemmerich and T. W. Hansch, Phys. Rev. Lett. **70**, 410 (1993).
- [23] J. P. Gordon and A. Ashkin, Phys. Rev. A **21**, 1606 (1980).
- [24] Ben Dahan M, Peik E, Reichel J, Castin Y and Salomon C, Phys. Rev. Lett. **76**, 4508 1996).
- [25] D. M. Stamper-Kurn , A. P. Chikkatur, A. Grlitz , S. Inouye, S. Gupta, D. E. Pritchard, and W. Ketterle Phys. Rev. Lett. **83**, 2876 (1999).
- [26] M.P.A. Fisher, P.B. Weichman, G. Grinstein, and D.S. Fisher, Phys. Rev. B **40**, 546 (1989).
- [27] D. Jaksch, C. Bruder, J.I. Cirac, C.W. Gardiner, and P. Zoller, Phys. Rev. Lett. **81**, 3108 (1998).
- [28] M. Greiner, O. Mandel, T. Esslinger, T. Hansch, and I. Bloch, *Nature* **415**, 30, (2002).
- [29] Thilo Stoferle, Henning Moritz, Christian Schori, Michael Kohl, and Tilman Esslinger, Phys. Rev. Lett. **92**, 130403 (2004).
- [30] D. van Oosten et. al. cond-mat/0405492 (2004).

- [31] P. Nozières and D. Pines, *The Thoery of Quantum Liquids*, Addison Wesley, Redwood City, CA (1990).
- [32] M. H. Anderson, J. R. Ensher, M. R. Matthews, C. E. Wieman, and E. A. Cornell, *Science* **269**, 198 (1995).
- [33] K. B. Davis, M. -O. Mewes, M. R. Andrews, N. J. van Druten, D. S. Durfee, D. M. Kurn, and W. Ketterle, *Phys. Rev. Lett.* **75**, 3969 (1995).
- [34] Peter J, Martin, Bruce, G. Oldaker, Andrew H Miklich, and David E. Pritchard *Phys. Rev. Lett.* **60**, 515 (1987).
- [35] J. Steinhauer, R. Ozeri, N. Katz, and N. Davidson *Phys. Rev. Lett.* **88**, 120407 (2002).
- [36] H. Palevsky, K. Otnes, and K. E. Larsson, *Phys. Rev. Lett.* **112**, 11, (1958).
- [37] F. Zambelli, L.Pitaevski, D.M. Stamper-Kurn, and S. Stringari, *Phys. Rev. A* **61**, 063608 (2000).
- [38] J.D. Miller, R.A. Cline, and D. J. Heinzen, *Phys. Rev. A* **47**, R4567 (1993).
- [39] J. Dalibard and C. Cohen-Tannoudji, *J. Opt. Soc. Am. B* **2**, 1707 (1985).
- [40] Wilhelm Zwerger, *J. Opt. B: Quantum Semiclas. Opt.* **5**, S9 (2003).
- [41] C. Menotti, M. Krämer, L. Pitaevskii and S. Stringari, {cond-mat/0404272.

- [42] D. Boers, C. Weiss and M. Holthaus, *Europhys. Lett.* **67**, 887 (2004).
- [43] Jan Gruenert, Master Thesis, University of Texas (1994).
- [44] T. Walker, D. Sesko, and C. Wieman, *Phys. Rev. Lett.* **64**, 408 (1990).
- [45] W. etterle, D.B. Davis, M.A. Joffe, A. Martin, and D.E. Pritchard, *Phys. Rev. Lett.* **70**, 253 (1993).
- [46] D. E. Pritchard *Phys. Rev. Lett.* **51**, 1336 (1983).
- [47] T. Bergeman, G. Erez, and H.Metcalf, *Phys. Rev. A* **35**, 1535, (1987).
- [48] E. Majorana. Atomi orientati in campo magnetico variabile. *Nuovo Cimento*, 9 ,43 (1933).
- [49] G. Baym and C.J. Pethick, *Phys. Rev. Lett.* **76**, 6 (1996).
- [50] Y. Castin and R. Dum *Phys. Rev. Lett.* **77**, 5315 (1996).
- [51] Changyun Ryu, Ph.D. Thesis, University of Texas (2004)
- [52] Ana Maria Rey et. al. [cond-mat/0406552](https://arxiv.org/abs/cond-mat/0406552)
- [53] Ehud Altman, Assa Auerbach *Phys. Rev. Lett.* **89**, 250404 (2002).
- [54] G.T. Zimanyi, P.A. Crowell, R.T. Scalettar, and G.G. Batrouni, *Phys. Rev. B* **50**, 6515 (1994).
- [55] M. Baert, V. V. Metlusho, R. Jonckheere, V. V. Moshchalkov, and Y. Bruynseraede, *Phys. Rev. Lett.* **74**, 3269 1995; K. M. Beauchamp, T. F.

- Rosenbaum, U. Welp, G. W. Crabtree, and V. M. Vinokur, Phys. Rev. Lett. **75**, 3942 (1995).
- [56] A. van Oudenaarden, and J.E. Mooij, Phys. Rev. Lett. **76**, 4947 1996
- [57] J. K. Freericks and H. Monien, . Lett. 26, 545 1994; Phys. Rev. B 53, 2691 (1996).
- [58] G. G. Batrouni, R. T. Scalettar, and G. T. Zimanyi, Phys. Rev. Lett. **65**, 1765 (1990).
- [59] P. Niyaz, R. T. Scalettar, C. Y. Fong, and G. G. Batrouni, Phys. Rev. B **50**, 362 (1994).
- [60] Subir Sachdev, *Quantum Phase Transitions*, Cambridge University Press (1999).
- [61] Thilo Stferle, Henning Moritz, Christian Schori, Michael Khl, and Tilman Esslinger, Phys. Rev. Lett. **92**, 130403 (2004).
- [62] C. Kollath, U. Schollwck, J. von Delft, and W. Zwerger, Phys. Rev. A **69**, 031601 (2004).
- [63] R. Roth and K. Burnett, Phys. Rev. A **67**, 031602(R) (2003).
- [64] Dries Van oosten, Ph.D. Thesis, Universiteit Utrecht (2004)
- [65] J. K. Freericks and H.Monien. Phase diagram of the Bose Hubbard model. *Europhys. Lett.* **26**, 545 (1995).

- [66] D. van Oosten, P. van der Straten, and H. T. C. Stoof. Quantum phases in an optical lattice. *Phys. Rev. A* **63**, 053601 (2001).
- [67] Yu. B. Ovchinnikov, J. H. Muller, M. R. Doery, E. J. D. Vredenburg, K. Helmerson, S. L. Rolston, and W. D. Phillips, *Phys. Rev. Lett.* **83**, 284 (1999).
- [68] R.H. Wynar, Ph.D. Thesis, The University of Texas (2000).
- [69] R. Wynar, R.S. Freeland, D.J. Han, C. Ryu, and D.J. Heinzen, *Science* **287**, 1016 (2000).
- [70] D. Jaksch, V. Venturi, J. I. Cirac, C. J. Williams, and P. Zoller, *Phys. Rev. Lett.* **89**, 040402 (2002).
- [71] J.D. Miller, R.A. Cline, and D.J. Heinzen, *Phys. Rev. Lett.* **71**, 2204 (1993).
- [72] C. Kollath, U. Schollwock, J. von Delft, and W. Zwerger, *Phys. Rev. A* **69**, 031601(R) (2004).
- [73] C. A. Regal, M. Greiner, and D. S. Jin, *Phys. Rev. Lett.* **92**, 083201 (2004).
- [74] M. Greiner, C. A. Regal, and D. S. Jin, *Nature* **426**, 537 (2003).
- [75] C. A. Regal, C. Ticknor, J. L. Bohn, and D. S. Jin, *Nature* **424**, 47 (2003).
- [76] P. G. H. Sandars, *Phys. Rev. Lett.* **19**, 13896 (1967).

- [77] L. N. Cooper, *Phys. Rev* **104**, 1189 (1956).
- [78] B. DeMarco and D. S. Jin, *Science* **285**, 1703 (1999).
- [79] G. Roati, F. Riboli, G. Modugno, and M. Inguscio, *Phys. Rev. Lett.* **89**, 150403 (2002).
- [80] A. G. Truscott, K. E. Strecker, W. I. McAlexander, G. B. Partridge, and R. G. Hulet, *Science* **291**, 2570 (2001).
- [81] F. Schreck, L. Khaykovich, K. L. Corwin, G. Ferrari, T. Bourdel, J. Cubizolles, and C. Salomon, *Phys. Rev. Lett.* **87**, 080403 (2001).
- [82] S. R. Granade, M. E. Gehm, K. M. O'Hara, and J. E. Thomas, *Phys. Rev. Lett.* **88**, 120405 (2002).
- [83] W. Hofstetter, J. I. Cirac, P. Zoller, E. Demler, and M. D. Lukin, *Phys. Rev. Lett.* **89**, 220407 (2002).
- [84] Gang Xu, Ph.D. Thesis, University of Texas (2001).
- [85] Z. T. Lu, K. L. Corwin, M. J. Renn, M. H. Anderson, E. A. Cornell, and C. E. Wieman, *Phys. Rev. Lett.* **77**, 3331 (1996).
- [86] Z. Hadzibabic, C. A. Stan, K. Dieckmann, S. Gupta, M.W. Zwierlein, A. Grilitz, and W. Ketterle, *Phys. Rev. Lett.* **88**, 160401 (2002).
- [87] W. Phillips and H. Metcalf, *Phys. Rev. Lett.* **49**, 1149 (1982).

- [88] Thomas E. Barrett, Samuel W. Daporeschwartz, Mark D. Ray, and Gregory P. Lafyatis, Phys. Rev. Lett. **67**, 3483 (1991).

## Vita

Emek Yesilada was born in Famagusta, Cyprus on November, 14 1977, the second son of Ali Fevzi Yesilada and Müzeyyen Yesilada. He attended the Turkish Maarif College High School and entered University of Rochester in 1994 on a Cyprus American Scholarship Program. He received his Bachelor of Science degree in Physics in May 1998. In August 1998, he entered the Graduate School of the University of Texas.

Permanent address: 3605 Steck Ave Apt. 2117  
Austin, Texas 78759

This dissertation was typeset with L<sup>A</sup>T<sub>E</sub>X<sup>†</sup> by the author.

---

<sup>†</sup>L<sup>A</sup>T<sub>E</sub>X is a document preparation system developed by Leslie Lamport as a special version of Donald Knuth's T<sub>E</sub>X Program.